

The CFHT Open Star Cluster Survey. III. The White Dwarf Cooling Age of the Rich Open Star Cluster NGC 2099 (M37)

Jasonjot Singh Kalirai¹

Paolo Ventura²

Harvey B. Richer¹

Gregory G. Fahlman^{1,3}

Patrick R. Durrell⁴

Francesca D'Antona²

and

Gianni Marconi⁵

ABSTRACT

We present deep CCD photometry of the very rich, intermediate aged (similar to the Hyades) open star cluster NGC 2099 (M37). The V , $B-V$ color-magnitude diagram (CMD) for the cluster shows an extremely well populated and very tightly constrained main-sequence extending over 12 magnitudes from the turn-off. Both a well defined main-sequence turn-off and a red giant population are also clearly evident. The CFH12K photometry for this cluster is faint enough ($V \sim 24.5$) to detect the remnants of the most massive progenitor cluster stars under the Type I SNe limit. Therefore, the CMD of the cluster also exhibits a well defined white dwarf 'clump' caused by the decreased rate of cooling of these stars as they age, and a subsequent gap with very few objects. By using source classification to eliminate faint-blue galaxies and a statistical subtraction technique to eliminate foreground/background objects, we have determined the age of

¹Department of Physics & Astronomy, 6224 Agricultural Road, University of British Columbia, Vancouver, BC V6T 1Z1; jkalirai@physics.ubc.ca, richer@astro.ubc.ca

²Osservatorio Astronomico di Roma, Sede di Monteporzio Catone, Via Frascati 33, I-00040, Italy; paolo@coma.mporzio.astro.it, dantona@coma.mporzio.astro.it

³Canada-France-Hawaii Telescope Corporation, P.O. Box 1597, Kamuela, Hawaii 96743, USA; fahlman@cfht.hawaii.edu

⁴Department of Astronomy & Astrophysics, Pennsylvania State University, 525 Davey Lab, University Park, PA, 16802, USA; pdurrell@astro.psu.edu

⁵European Southern Observatory, ESO-Chile, Casilla 19001, Santiago, Chile; gmarconi@eso.org

the star cluster from the termination point ($M_V = 11.95 \pm 0.30$) in the white dwarf luminosity function. The white dwarf cooling age is found to be 566 ± 154 Myrs from comparisons with white dwarf cooling models and is in excellent agreement with the main-sequence turn-off isochrone age (520 Myrs). After carefully accounting for the uncertainties in the white dwarf limiting magnitude, we show that the cooling age confirms that models including convective core overshooting are preferred for young-intermediate aged clusters. This is particularly important in the case of NGC 2099 as the age is similar to that of the Hyades cluster, for which current models have difficulties in reproducing the details of the main-sequence turn-off. We also derive the reddening ($E(B-V) = 0.21 \pm 0.03$) and distance ($(m-M)_V = 11.55 \pm 0.13$) to NGC 2099 by matching main-sequence features in the cluster to a new fiducial main-sequence for the Hyades, after correcting for small metallicity differences. As a continuing part of the goals of the CFHT Open Star Cluster Survey to better understand dynamical processes of open clusters, we also fit a King model to the cluster density distribution and investigate the cluster main-sequence luminosity and mass functions in increasing concentric annuli. We find some evidence for mass segregation within the boundary of NGC 2099 as expected given the cluster's age relative to the dynamical age. The present global mass function for the cluster is found to be shallower than a Salpeter IMF.

Subject headings: color-magnitude diagrams – open clusters and associations: individual (NGC 2099) – stars: evolution – stars: luminosity function, mass function – white dwarfs

1. Introduction

White dwarfs represent the end point in the life of low mass stars ($M \lesssim 7 M_\odot$). These burnt out stellar cinders have extinguished their nuclear fuel and are now radiating away any remaining stored thermal energy. Younger than an age of about 8 Gyrs, white dwarfs will simply cool and fade, becoming dimmer and redder as time passes. White dwarfs typically have $10 \lesssim M_V \lesssim 17.5$ (depending on the age of the star), making them difficult to detect at moderate distances. This primary deterrent has prevented the establishment of observational constraints on certain theoretical aspects of white dwarfs. For example, constraints on both the initial-final mass relationship for white dwarfs and the upper mass limit for white dwarf production are very limited (Weidemann 2000, 1987; Reimers & Koester 1988b). A progenitor-white dwarf initial-final mass relationship is particularly important for Galactic chemical evolutionary studies as it would provide important information on the amount of stellar mass loss in post main-sequence evolutionary stages.

Star clusters represent at least a partial solution to the difficulties in studying white dwarfs and they provide an excellent environment in which we can learn more about the properties of these

objects. The assumed single-burst star formation event that creates a star cluster produces stars with a spectrum of masses yet similar metallicity, age and (most importantly) distance. Since the evolution of stars is driven primarily by their initial mass, examining different populations of stars in a cluster can give us a snapshot of the life stages of a single star: turn-off, red giant, planetary nebula, white dwarf, etc. (see Renzini & Fusi-Peccia 1988). By applying a statistical argument to objects in different locations of a cluster CMD, we can infer information about the properties of objects in different stellar evolutionary stages, such as white dwarfs. Studying white dwarfs in practice, however, is not this simple. The richest star clusters, the globular clusters, contain large numbers of white dwarfs but these clusters are also very old. Therefore the limiting magnitude of the coolest white dwarfs in these clusters occurs at magnitudes that are too faint for ground based observations. For example, the limiting white dwarf magnitude for a 12 Gyr cluster occurs at $M_V = 17.5$ (Richer et al. 2000). The only program currently underway to establish the white dwarf cooling age of a globular star cluster is a deep HST study of M4, the nearest globular cluster (Richer et al. 1997). Success in this study may be possible because it takes advantage of new models that predict radically different behavior in the emergent spectra of cool white dwarfs with ages $\gtrsim 8$ Gyrs or $T_{\text{eff}} \lesssim 4000$ K (Hansen 1999; Saumon & Jacobson 1999).

An alternative method of studying white dwarfs is to utilize the much younger and more metal-rich open star clusters. These systems are found over a very broad range of parameters such as distance, age, metallicity and richness. However, there are also difficulties in using open star clusters to study white dwarfs. First, the clusters are confined to the disk of the Milky Way so background contamination is large. For poorly populated clusters, this makes it very difficult to distinguish the cluster population from the background. The interpretation of the photometry for many open clusters is also difficult due to heavy extinction and reddening of star light. Second, most open clusters are large in angular extent ($\sim 20'$), so there are many background galaxies in the field of view. Some of these will appear as faint, blue objects, thereby mimicking white dwarfs. Thirdly, because open clusters are confined to the disk, tidal interactions from giant molecular clouds work to dissipate the clusters as they orbit the Galaxy. Wielen (1991) shows that a moderately rich open cluster in the solar neighborhood consisting of 500 stars ($\sim 250 M_{\odot}$) will dissolve in a timescale of about 2×10^8 years.

What we require to address the properties of white dwarf stars are very rich, yet intermediate aged open star clusters with little reddening. The clusters must be old enough so that a significant number of white dwarfs have formed, yet young enough so that the end of the white dwarf cooling sequence occurs at an observable magnitude. Although NGC 2099 has a low Galactic latitude ($b^{II} = 3.1^\circ$) and consequently a moderately high reddening value ($E(B-V) = 0.21$), it is an excellent cluster for white dwarf studies because of its extremely rich stellar population (our photometry detects 2620 stars) and its intermediate age (~ 500 Myrs).

NGC 2099 was established as a relatively rich and large star cluster very early on and thus has been the focus of many studies, for example: photometrically by von Zeipel & Lindgren (1921); Becker (1948); Hoag et al. (1961); spectroscopically by Zug (1933); Lindblad (1954); and astromet-

rically by Nordlund (1909); Giebel (1914); Lindblad (1954); Upgren (1966) and Jeffreys (1962). The first significant photometric study that shed light on cluster parameters was that of West (1967). West used photographic plates to establish a CMD for 930 member stars brighter than $V = 17.7$. The photometric spread in the cluster main-sequence from this study is quite large and consequently, there are large uncertainties in the results. That UBV study concluded with an estimated cluster age of 220 Myrs, distance modulus of $(m-M)_V = 11.6$, and a constant reddening value of $E(B-V) = 0.27$. The first significant dynamical study of the stellar density distribution around the area of NGC 2099 was based on three-color Schmidt plate photometry in 1975 (Becker & Svolopoulos 1976). The latest study of the cluster used radial velocity and UBV photoelectric observations to establish a much cleaner main-sequence based on cluster membership (Mermilliod et al. 1996). The results of this study concluded with $(m-M)_V = 11.5$, $E(B-V) = 0.29$, age = 450 Myrs (comparison to theoretical isochrones from Schaller et al. (1992) and Bertelli et al. (1994)) and $Z = 0.020$. The CMD of this study exhibits less than 100 objects and has a limiting magnitude brighter than $V = 17$. The quality of the data in the present study is unprecedented when compared with these previous efforts (see Figure 5 for a comparison of CMDs).

In the next section we discuss the instrumentation that was used to collect this data and the photometric reduction procedures. We then present the cluster CMD which exhibits a very tight main-sequence stretching over 12 magnitudes in the V , $B-V$ plane, consisting of more than 2600 stars. We derive the reddening and distance modulus to NGC 2099 by comparing the un-evolved main-sequence to a new fiducial for the Hyades star cluster (de Bruijne, Hoogerwerf & de Zeeuw 2001). We also draw comparisons, both on the observational and theoretical planes, to the Hyades cluster which has a similar age to NGC 2099. This age estimate is determined by fitting the main-sequence turn-off and the luminosity of the red giant clump with up-to-date theoretical stellar evolutionary sequences, calculated especially for the CFHT Open Star Cluster Survey (Kalirai et al. 2001a, hereafter Paper I). An analysis of dynamical effects in the cluster is discussed in §§4.2 and 5. The cluster mass function is derived in §6 and the corresponding total mass of the cluster is corrected for those stars between our limiting magnitude and the hydrogen burning limit in §7. Finally, we conclude by presenting studies of potential white dwarf stars in NGC 2099 and determining the white dwarf cooling age of the cluster (§8).

2. Observations and Reductions

Most of the observational data for NGC 2099 was obtained during the second night of a three night observing run in 1999 October, using the CFH12K mosaic CCD on the Canada-France-Hawaii Telescope. This CCD contains 12, 2048×4096 pixel ($0''.206$) chips that project to an area of $42' \times 28'$ on the sky. This is larger than the apparent cluster radius of $\sim 13'.9$ (see §4.2). We obtained three 300-second images in both B and V, as well as single 50 and 10-second images in each of the B, V and R filters. At a later date, we also acquired short 0.5-second frames to obtain unsaturated images of the bright stars in the cluster (see Table 1). Blank field images are not necessary as

the outer regions of the mosaic can be used to correct for field star and galaxy contamination. Most images were obtained while the sky was photometric with sub-arcsecond seeing conditions (see Table 1). A color image created from the deep V and B images is shown in Figure 1.

The data was processed (flat-field, bias and dark corrected) and montaged using the FITS Large Images Processing Software (FLIPS) (Cuillandre 2001) as described in §3 of Paper I. In the final processed images, we find the flat-fielding to be good to $\sim 0.5\%$ in V and $\sim 0.7\%$ in B, averaged over 11 \square'' patches. We reduced the data using a preliminary version of the new TERAPIX photometry routine PSFEx (Point Spread Function Extractor) (E. Bertin 2000, private communication). We used a separate, variable PSF for each CCD in the mosaic. The mean errors in the photometry were 0.015 mag at V = 22, 0.032 mag at V = 23 and 0.075 at V = 24. A statistical error plot is shown in Figure 2. Further information on PSFEx can be found in §4 of Paper I. Numerous photometric calibration frames of Landolt fields SA-92 and SA-95 (Landolt 1992) were used to calibrate the NGC 2099 data (see Tables 2 and 3 in Paper I). Calibration methods are discussed in §§5.1 and 5.2 of the same paper. The photometric uncertainty in the zero points for the standard stars during night 2 were measured to be ~ 0.021 in V and ~ 0.025 in B. The extinction in magnitudes per airmass was determined to be 0.084 ± 0.012 in V and 0.184 ± 0.008 in B, both close to the standard CFHT values of 0.10 and 0.17 respectively and similar to those on the first night of the run (0.088 ± 0.010 in V and 0.165 ± 0.005 in B). The color terms were averaged over the three night observing run and found to be in agreement with CFHT estimations in the V filter and slightly lower than estimations for the B filter.

3. The NGC 2099 Color-Magnitude Diagram

In Figure 3 we present CMDs for both the cluster and a background field after applying a 0.50 stellarity cut from SExtractor (Bertin & Arnouts 1996) to remove obvious faint galaxies (see §3.1). The cluster field in this Figure has been scaled down in area to be consistent with the area represented in the background field (i.e. each object in the background field represents 1.37 cluster field objects). This has been done by eliminating a ring of objects centered close to the half-mass radius (4.5 pc) of the cluster (a full CMD consisting of the entire cluster population is presented later, Figure 5). The cluster CMD shows a magnificent tightly constrained main-sequence extending over 12 magnitudes from the cluster turn-off $V \sim 12$ ($M_V = 0.45$) to $V \sim 23.5$ ($M_V = 11.95$). A tight red giant clump is seen consisting of 20 stars (see Figure 5 for all stars). There is also a significant background disk star population below the main-sequence in the cluster CMD and in the background field. This distribution arises due to the low Galactic latitude of the cluster and clearly overlaps significantly with the faintest cluster members on the CMD. In fact, the feature in the background field at $20 \leq V \leq 23.5$ and $B-V \sim 1.7$ (which can also be seen in the NGC 6819 data set) may in part be faint cluster red stars located between our apparent cluster radius (the limit to which we can detect cluster stars) and the tidal radius (see §4.2).

The cluster CMD in Figure 3 also shows several faint, blue objects that will be discussed in

detail in §8. Although there is field star and background galaxy contamination, the density of objects is clearly greater in the cluster CMD indicating that a significant number of these objects are cluster white dwarf members (see §8.1 for statistical arguments involving the subtraction of field stars and removal of galaxies). These stars have quickly evolved ($\sim 10^4$ – 10^5 years) from the red giant phase to the white dwarf phase and are now slowly piling up on the CMD at a magnitude that can be used to independently infer the cluster age. The NGC 2099 CMD clearly shows the faintest objects in this ‘clump’ to be at $V = 23.5$, after which point there is a significant gap signifying that we have detected the termination point in the white dwarf cooling sequence (the complete CMD in Figure 5 shows this better). We also note that the photometry for these bluer objects is fainter than for the main-sequence by over 1 magnitude.

The cluster CMD (from Figure 5) also shows several (5) very blue and bright objects, some of which may in fact be stars that have shed their outer layers during the planetary nebula stage and are now cooling to become white dwarfs. We do not expect to detect many, if any, objects at this stellar evolutionary stage because the stars spend a very small amount of time during this phase. A crude estimate of the expected number of such objects can be determined by comparing the evolutionary time ($\lesssim 10^5$ years) of these stars to the numbers (20) and timescales (100 Myrs) of red giants in the clump of NGC 2099. Although the theoretically expected number is less than one, three of the objects in the CMD are centrally concentrated in the cluster, not image defects, and have a high stellarity index. Spectroscopic confirmation is needed to determine whether any of these objects are cluster members and potentially among the most interesting stars in NGC 2099. If confirmed, these objects would provide crucial observational constraints on the phases of evolution from the planetary nebulae stage to the white dwarf stage (Iben & Renzini 1983) and on neutrino cooling of pre-white dwarf stars (O’Brien et al. 1998).

3.1. Stellarity

We use source classification to distinguish between stars and galaxies at faint magnitudes where the signal-to-noise ratio is low. The star/galaxy cut will affect both evolutionary tests of stars that become white dwarfs and the luminosity function for these stars. We use SExtractor to assign a stellarity index to all objects on all CCDs in our data. This stellarity index is determined through a robust procedure that uses a neural network approach as described in Bertin & Arnouts (1996).

Figure 4 shows the variation of this stellarity index with magnitude. There is a clear group of both resolved sources (stellarity = 0) and unresolved (stellarity = 1). Additionally, we have visually inspected and determined that most of the objects in the ‘clump’ between $23 \leq B \leq 24.5$ and $0.75 \leq \text{stellarity } B \leq 0.95$ are most likely stars. The determination is more difficult for objects with lower stellarity. Previous experience (Kalirai et al. 2001b, hereafter Paper II) has shown that a 0.50 stellarity cut may not be stringent enough whereas a 0.75 stellarity cut may be eliminating too many stellar sources. For now, we will employ a 0.50 stellarity cut (in all Figures) so as to not remove any truly stellar objects. This cut will be justified in §8.1.

3.2. Cluster Metallicity

An ideal testing of theoretical stellar isochrones by using observational CMDs requires prior knowledge of the cluster metallicity, reddening and distance. Unfortunately, prior NGC 2099 data have not set tight constraints on any of these. Although the published literature does not show any detailed spectroscopic abundance studies of the cluster, Lynga's Fifth Catalogue of Cluster Parameters (see e.g., Janes, Tilley & Lynga 1998) lists the cluster metallicity to be $[Fe/H] = 0.09$ or $Z \sim 0.020$. Additionally, the study of Mermilliod et al. (1996) experimented with different models (Schaller et al. 1992 and Bertelli et al. 1994) and examined the colors of the red giant clump in NGC 2099 also concluding with a best fit $Z = 0.020$ isochrone. Since there have been no studies contradicting this metallicity, we adopt the $Z = 0.020$ value as the most likely cluster metallicity, but will also consider a $Z = 0.025$ (Hyades-like (Perryman et al. 1998)) value (see §3.4.2).

3.3. Cluster Reddening and Distance – Main-Sequence Fitting with the Hyades

The only previous model-independent reddening estimate of NGC 2099 comes from the photographic work of West (1967), $E(B-V) = 0.27$. The main sequence of these data contains a large scatter. The color-color plots also suffer from large uncertainties (photometric spread ~ 0.5 magnitudes in $B-V$). The study of Mermilliod et al. (1996) compared their photoelectric data to stellar isochrones and estimated the reddening to be $E(B-V) = 0.29$. The advantages of determining a reddening value from the present data over the previous works include the higher stellar density, deeper CMD and lower uncertainties in the photometry. See Figure 5 for a comparison of the present CMD with these studies and Figure 6 for a residual star-by-star comparison with the photoelectric data. Unfortunately, the R filter photometry for NGC 2099 was unable to provide reddening constraints as the slope of the reddening vector ($E(V-R)/E(B-V) = 0.78$) is too similar to the observed sequence in the color-color plot. An accurate UBV or BVI analysis is desirable for the cluster.

An alternative method of determining the reddening of a star cluster was demonstrated in the analysis of M4 (Richer et al. 1997), where a set of subdwarf stars were fit to the observed main-sequence to simultaneously solve for both the reddening and apparent distance modulus. Due to the degeneracy between these two quantities, the results established more stringent ranges on the reddening than for the apparent distance modulus. We adopt a similar technique by using the well established Hyades main sequence to fit NGC 2099. This method is ideal for the present comparisons due to the long main sequences of the two clusters (stars with mass below $2.6 M_{\odot}$ in NGC 2099 have not yet evolved off the main-sequence), accurate photometry (several observable features are present in both main-sequences), similar metallicity of the clusters ($Z = 0.024$ for Hyades) and similar age for the clusters (see §3.4.2).

The new fiducial main-sequence of the Hyades open star cluster is based on a new analysis of Hipparcos individual parallaxes by de Bruijne, Hoogerwerf & de Zeeuw (2001). The fiducial was

calculated by binning known cluster members at 0.5 magnitude intervals from $M_V = 1.5$ to $M_V = 9$ with a small color cut to remove outliers. Binaries were removed, however we include the brightest binary component which defines the turn-off of the cluster (star $\theta^2\tau_A$). We first adjust the NGC 2099 CMD by $+0.03$ in $B-V$ to account for the $\Delta Z \sim 0.005$ metallicity difference in the clusters. We then compare observable features in our tight main-sequence, such as the ‘kink’ in the main-sequence at $(B-V)_o \sim 0.4$ caused by changes from convective envelope models to radiative envelopes, as well as the general shape and slope of the main-sequence to the Hyades fiducial ($E(B-V) = 0.003 \pm 0.002$, mean $(m-M)_V = 3.27$) to solve for the best combination of reddening and apparent distance modulus. The results point towards a reddening of $E(B-V) = 0.23 \pm 0.03$ and an apparent distance modulus of $(m-M)_V = 11.65 \pm 0.13$, where the uncertainty in the latter value reflects the range of main-sequence fitting distance moduli obtained by using reddening values at the extremes of the ± 0.03 uncertainty. Figure 7 illustrates the remarkable agreement between the detailed features of the two main-sequences for these values. Additional reddening constraints are also provided by comparing the colors of the NGC 2099 red giant clump to the Hyades clump (which is reproduced well by our current theoretical models). The small age difference between the two clusters (see §3.4.2) would affect the luminosity of the clump stars significantly, but only slightly affect the color. On this metallicity corrected plane, the clump of NGC 2099 can not be redder than the Hyades (would imply $Z \gtrsim 0.024$), however for a reddening value $E(B-V) \lesssim 0.18$, this condition is violated and therefore such a low reddening can be ruled out.

Given the uncertainties in the reddening, distance modulus, metallicity and model colors (discussed in §3.4.2) we incrementally massage the reddening by -0.02 to allow a slightly better isochrone fit of the model to the un-evolved main-sequence of NGC 2099. Therefore, our best estimate of the reddening of NGC 2099 is $E(B-V) = 0.21 \pm 0.03$, with a corresponding distance modulus of $(m-M)_V = 11.55 \pm 0.13$. The uncertainties in these values are not known well enough to establish different upper and lower limits based on the adjustment from the main-sequence fitting values. The higher limits established earlier are ruled out by the models so to remain consistent we will use the model-massaged values throughout. With the lower adopted reddening value, this distance modulus is in good agreement with the value of West ($(m-M)_V = 11.64 \pm 0.1$) and Mermilliod ($(m-M)_V = 11.50$). The agreement with the Hyades cluster using the new reddening and distance modulus is slightly worst than for the best main-sequence fitting values. This is most likely due to the metallicity of the cluster not being exactly $Z = 0.02$. The corresponding distance to NGC 2099, using $A_V = 3.1E(B-V)$, is 1513 ± 133 pc. The error in the true distance modulus (10.90 ± 0.16) combines four individual errors, and accounts for correlations between them: (1) a scale factor translation ($\Delta(B-V)$ to ΔV) from the $B-V$ axis to the V axis to account for the reddening uncertainty, (2) an estimated main-sequence fitting uncertainty at a fixed reddening value, (3) the error in the extinction, $\Delta_{A_V} = 3.1\Delta_{E(B-V)}$ and (4) the color uncertainty due to an estimated metallicity uncertainty, Δ_Z . We evaluate and provide a more detailed description of these terms in §8.4.

3.4. Theoretical Isochrones

3.4.1. Model Description

The theoretical models that we will use for this project have been calculated especially for the CFHT Open Star Cluster Survey at the Rome Observatory and are up-to-date in the input physics. A detailed description of the stellar evolution code that was used to build the tracks can be found in Ventura et al. (1998) (also see §5.2 of Paper II). We assume that the helium abundance scales with the metallicity content according to the relation $\Delta Y/\Delta Z = 2$. The models adopt convective core-overshooting by means of an exponential decay of turbulent velocity out of the formal convective borders as fixed by Schwarzschild's criterion; this behavior of velocity is consistent with approximate solutions of the Navier-Stokes equations (Xiong 1985), and with the results of numerical simulations (Freytag et al. 1996). A value of $\zeta = 0.03$ for the free parameter giving the e-folding distance of the exponential decay has been adopted (Ventura et al. 1998). The convective flux has been evaluated according to the Full Spectrum of Turbulence (FST) theory prescriptions (Canuto & Mazzitelli 1992). The theoretical isochrones were transformed into the observational plane by making use of the Bessell et al. (1998) conversions. The lower main sequence ($M \lesssim 0.7 M_{\odot}$) has been calculated by adopting NextGen atmosphere models (Hauschildt, Allard & Baron 1999). Models based on a grey atmosphere approximation give almost identical results for larger masses. For $M \lesssim 0.47 M_{\odot}$ (or $T_{\text{eff}} \lesssim 3500$ K) the transformations of Hauschildt, Allard & Baron (1999) in $B-V$ are not very reliable and so the faint end of the isochrones terminate at this mass. However, the bolometric correction for cooler stars in the models can still be used to establish a mass-luminosity relationship extending to $M \sim 0.25 M_{\odot}$ (this is used in §6).

3.4.2. Observation vs. Theory

Comparing the observed NGC 2099 CMD with stellar isochrones can not only provide an age for the cluster, but can also allow for refinements in the models and a better understanding of the theory of stellar evolution. Figure 8 shows three panels with two isochrones assuming extra mixing beyond the formal convective borders, but for different ages, and one isochrone calculated assuming no extra mixing. We argue the best fit in Figure 8 is in the left panel (520 Myrs - assuming core-overshooting) and for this combination of reddening, distance, metallicity and age, the isochrone reproduces several features of the CMD nicely. Several comparisons can be drawn from the fit of the theory to the observations. First the lower main-sequence in NGC 2099 is clearly redder than the isochrone. This slope change in the main-sequence, caused by the onset of H_2 dissociation-recombination in the stellar envelope (Copeland, Jensen & Jorgensen 1970) is not reproduced well by stellar models employing grey atmosphere boundary conditions (see e.g., Castellani, Degl'Innocenti & Prada Moroni 2001 for the lower main-sequence of the Hyades). The non-grey boundary conditions employed in our models for the lower main-sequence (J. Montalban 2001, private communication) are in better agreement with the general shape of the main-sequence,

but the models are still too blue by ~ 0.05 mag in B–V. This disagreement can be explained in part due to the use of the Bessell et al. (1998) colors at such low temperatures. Photometric spread in the data for faint stars may also partly contribute to such an effect. Also, the turn-off of NGC 2099 falls slightly redder than the model, although the shape is consistent with the data. Despite considerable effort, we find it difficult to reproduce the details of this feature in the NGC 2099 CMD with current models (while maintaining a good fit to the luminosity of the red giant clump). The problem here is very similar to that for the Hyades cluster, for which several groups are unable to provide a good fit to the turn-off. An extensive discussion concerning the difficulty of fitting both the turn-off and the lower main sequence region of the Hyades by adopting the same set of color-temperature calibrations can be found in de Bruijne, Hoogerwerf & de Zeeuw (2001). The fact that the NGC 2099 data is in excellent agreement with the Hyades data (see Figure 7), and models fail to reproduce the turn-off feature in both clusters, will motivate a deeper understanding of this feature of the CMD for intermediate aged clusters. Conversely, both the color and luminosity of the red giant clump are in excellent agreement with the data; the latter provides the age. The shape and slope of the main-sequence (from $M_V = 2.5 - 8.0$) is also in excellent agreement with this model. For example, the ‘kink’ in the main-sequence at $\sim 1.3 M_{\odot}$ described earlier is modelled perfectly. The age estimate of 520 Myrs for NGC 2099 is also consistent with Figure 7 which shows both the peel-off of the main-sequence stars in the Hyades (age ~ 600 Myrs with our models) and the luminosity of the clump stars to be slightly fainter than that for the corresponding stars in NGC 2099.

Fitting exactly the location of the turn-off region of the cluster requires a slightly higher age. The middle panel of Figure 8 shows the fit for an age of 580 Myrs. The shape of the turn-off of the cluster, as well as the hook at the top of the main-sequence caused by the contraction of stars that have exhausted their hydrogen supply (very difficult to see), are both modelled well. However, a close examination of the luminosity of the red giant clump shows a discrepancy of ~ 0.20 magnitudes. Given the importance and relative simplicity of fitting the clump luminosity rather than the turn-off, we believe this to be a poorer fit than that presented in the left panel.

Due to the uncertainty in the reddening value established in §3.3, we also note that we can not completely rule out ages as low as 450 Myrs for NGC 2099 (the value found by Mermilliod et al. (1996)). Using a reddening value near our upper limit ($E(B-V) \sim 0.25$), we obtain a decent fit to the luminosity of the clump stars, however, the subsequent fit to the main-sequence for this reddening is poor.

We also examined the possibility of fitting the observed NGC 2099 stars with an isochrone of metallicity $Z = 0.025$. For this, we derived the reddening and distance modulus by comparing the NGC 2099 main-sequence with the Hyades fiducial with no metallicity shift. The corresponding best fit to the luminosity of the clump is obtained for an age of ~ 550 Myrs. The NGC 2099 clump is brighter and slightly redder than the Hyades clump, indicating a younger age for NGC 2099 with respect to the Hyades. The fit to the slope of the main-sequence for this metallicity is clearly worse than for a $Z = 0.020$ model.

As we will discuss later in §8, one of the possible uses of white dwarfs as chronometers is to check the consistency of the turn-off and white dwarf ages. If we fit the cluster CMD with theoretical isochrones based on stellar models of the same metallicity ($Z = 0.020$), but calculated assuming no extra mixing beyond the formal convective borders, the best agreement between the theory and observations is obtained for an age of ~ 300 – 350 Myrs, using the same distance modulus and reddening as in the overshooting case. In this case, which is based on reproducing the luminosity of the clump, we get a very poor fit to the turn-off region, which is noticeably bluer than the observed stars (see right panel of Figure 8). An age of ~ 400 – 450 Myrs would lead to an acceptable fit of the turn-off of the cluster, but in this case the theoretical luminosity of the clump would be ~ 0.4 magnitudes fainter than the observed clump stars, a gross disagreement.

Finally, we tested to see what derived age would result for NGC 2099 from using the latest Padova group isochrones (Girardi et al. 2000). For their models with $Z = 0.019$ and $Y = 0.273$ (close to our values), we find a good fit to the general main-sequence using our derived cluster reddening and distance modulus. The best age however, is slightly younger (480 Myrs). This is most likely due to a slightly lower metallicity in their models and a different treatment of convection (a scaled overshooting parameter based on the turn-off mass). The theoretical clump in the Padova models is redder and fainter than the data (which again results from a different description of convection).

The above comparisons suggest that a certain amount of overshooting from the border of the convective core is required and that a solar metallicity ($Z = 0.020$) model of age 520 Myrs provides the best fit to the observed NGC 2099 CMD (based on the luminosity of the clump). However, a slightly larger age provides a better fit to the turn-off of the cluster. Models without convective core overshooting do not reproduce the observed data well. Ultimately it is the white dwarf cooling age of the cluster that will be the decisive discriminant (see §8.3).

4. Star Counts

4.1. Center of the Cluster

Star counts in concentric annuli around a cluster require a determination of the center of the cluster. To estimate this, we produced a histogram of star counts in thin strips across the mosaic. The center, in each of the x and y directions, was estimated from the center of the profile. The results give coordinates $\alpha_{J2000} = 05^h 52^m 17.6^s$, $\delta_{J2000} = +32^\circ 32' 08''$ which however are limited in accuracy to about $30''$. The uncertainty arises because of the large amount of scatter in the resulting plots (small number statistics).

4.2. Radial Density Distribution

Figure 9 shows the number of stars in increasing concentric annuli around NGC 2099, normalized by the area of each annulus. The annuli used are each $2'$ in width. The background field star population has been removed by scaling the counts in the background field (taken from the outer four CCDs surrounding the cluster – 14.4 stars/ \square') to the area of each annulus. To avoid significant incompleteness biases, only stars with $V \leq 22$ have been used. Also shown is a single mass King model (King 1962, 1966) which is found to fit the data well. We fit the model to the data by varying the concentration parameter ($\log(r_t/r_c)$) until the best fit is obtained. This allows us to determine the core radius, $r_c = 2.3$ pc, which strictly speaking has no physical meaning. The model then gives us the tidal radius, $r_t = 20.4$ pc, which is caused by tidal influences of massive objects in the Milky Way (e.g., GMCs) that remove the highest-velocity stars from the cluster as they venture out to large distances from the center. Finally, we compare the tidal radius from the model to the expected tidal radius of the cluster given the cluster's mass and it's position in the Galaxy (Binney & Tremaine 1987),

$$r_t \sim \left(\frac{m}{3M}\right)^{1/3} D. \quad (1)$$

The mass of the cluster in this calculation ($m = 2515 M_\odot$) has been corrected by including those stars between our faintest magnitude bins and the hydrogen burning limit ($0.08 M_\odot$) as described in §7. M is the mass of the Galaxy within the cluster's orbit (1.02×10^{11} – Clemens (1985)) and D is the Galactocentric distance of NGC 2099 (~ 10 kpc, almost directly towards the anti-center of the Milky Way). Solving equation 1 for the tidal radius of NGC 2099 gives $r_t = 20.2$ pc, in excellent agreement with the model value.

The apparent cluster radius of NGC 2099 is only ~ 6 pc and therefore some stars may have evaporated past this radius towards the outer parts of the cluster (this may in part be an explanation for the faint, red feature in the background CMD – see Figure 3). Such an effect would be important as it would bias the faint end luminosity function. We use the King model to determine the total mass of NGC 2099 out to the tidal radius of the cluster. This involves calculating the projected central density of the cluster as well as several model dependent parameters (see Gunn & Griffin 1979). This value is found to be $2548 M_\odot$ and is in excellent agreement with the value found by integrating the mass function to our limiting radius ($2515 M_\odot$ – see §§6 and 7). Further discussion of the dynamical state of the cluster can be found in §5.3.

5. Luminosity Functions

The rich stellar population of NGC 2099 motivates star count studies to determine the cluster population, its dynamical state, and investigate the luminosity and mass functions. The shape

of the luminosity function for this cluster is very important to establish observational constraints on the timescales and levels at which we expect dynamical evolutionary effects in clusters to take place. Dynamical effects in clusters are caused by equipartition of energy between stars of different masses. Although the concentration of stars for any mass will be highest in the center of the cluster and decrease as a function of radius from the center (Binney & Tremaine 1987), as the cluster ages we can expect the density distribution to expand from the center. The low mass stars will gain energy in the interactions and have higher velocity dispersions than the high-mass stars, which sink to the center of the cluster. The relaxation timescale is proportional to the number of crossings of a star across the cluster that are required for its velocity to change by order of itself (Binney & Tremaine 1987). Using the distance (1.5 kpc), population size (see §7), linear size (6.2 pc) and mass (see §7) of NGC 2099, we determine the relaxation time (see equation 2) to be ~ 300 Myrs,

$$t_{relax} \sim t_{cross} \frac{N}{8 \ln N}. \quad (2)$$

Therefore, we can expect the cluster (age ~ 500 Myrs) to be relaxed and exhibit some dynamical effects such as an excess of lower mass stars in the outer regions of the cluster. In fact, if old enough the cluster may even lose some stars due to these and other external processes such as tidal interactions in the disk of the Galaxy (Wielen 1991).

We define the cluster stars by first creating a main-sequence fiducial (clipping objects with $(B-V) \geq 3.5\sigma$ from the mean) after isolating the main-sequence from the background distribution (see Table 2). We then use a clipping routine to create an envelope around this fiducial based on the errors in the photometry (envelope broadens out towards faint magnitudes). The counting of the stars is done within this envelope, for both the cluster CMD and the background CMD, with the raw cluster luminosity function coming from the difference between the counts in the two fields (after accounting for aerial differences - see next section).

5.1. Incompleteness Corrections and Counting Uncertainties

Before we can interpret results from the star counts in NGC 2099 we must correct our data for incompleteness in the number of detected objects. This effect is typically negligible for brighter objects and increases for fainter sources. We produce an artificial catalogue of input stars for which we know the magnitudes and colors. A small number of these stars is added uniformly in several trials (7) in proportion to their numbers in the raw cluster luminosity function so as not to affect the crowding statistics of the field. These stars are chosen along the same slope of the main-sequence, and a separate sequence for the location of the white dwarfs. After adding these stars to our data frames, we re-reduce the new data in an identical manner to the original data in the cluster. This involves running PSFEx on the data and merging the output V and B files. We then count the number of stars per magnitude bin that were recovered (in both V and B).

This analysis is carried out for 2 cluster CCDs and 2 background field CCDs in order to make the analysis reliable. The cluster CCDs represent 2 of the central chips of CFH12K, and provide statistics on a $14' \times 14'$ region near and including the central core of NGC 2099. Each of the background field CCDs represent a $14' \times 7'$ area taken on opposite sides of the cluster. The NGC 2099 data set is found to be 100% complete down to $V = 19$ in the background field and 100% complete to $V = 17$ in the cluster field. For main-sequence stars the correction at $V = 22.5$ in the cluster field is 1.219 (i.e. $N_{\text{added}}/N_{\text{recovered}} = 1.219$). The white dwarfs are more complete than the main-sequence stars in almost all bins. This is expected as these stars are brighter in the B band for a given V band magnitude than the main-sequence stars. A summary of the incompleteness factors for the 2 cluster and background field CCDs is given in Table 3.

The errors in the incompleteness corrections are evaluated using an identical analysis to that described by Bolte (1989) and implemented in Paper II. Namely, we assume that the counting uncertainties are derived from a Poisson distribution and that the artificial star count uncertainties are derived from a binomial distribution. Furthermore, the errors in the incompleteness and the raw star counts are assumed to be uncorrelated. The errors from the cluster and background fields are added in quadrature.

The completeness-corrected number of stars in the cluster can now be determined in three steps. First, we multiply the cluster field incompleteness correction by the number of stars in the cluster in that magnitude range. Second, we multiply the background field incompleteness correction by the number of background field stars, and multiply the result by 1.37 to account for the difference in aerial coverage of the background. Finally, we subtract the two and obtain the corrected star counts. For the global star counts, we use the inner $13.9'$ for the cluster field and establish a background field area from the outer portions of the outer CCDs. The cluster density at this radius has dropped off significantly from the central regions, however, in the absence of a strong field star population, cluster members could have been detected at greater radii.

The final corrected star counts are presented in Table 4. In this table, the first row of each magnitude bin consists of raw counts (cluster field – $1.37 \times$ background field) whereas the row underneath contains the incompleteness corrected numbers (correction applied from Table 3). Also shown in parentheses are the errors in these counts, as calculated from the analysis given above.

5.2. Analyzing the Cluster Luminosity Function

The global luminosity function for NGC 2099 is plotted in Figure 10, where the dashed line represents the raw counts and the solid line the incompleteness corrected counts. The global luminosity function is almost flat from $V = 13.5$ ($M_V \sim 2$) to $V = 19.5$ ($M_V \sim 8$) and slowly rises beyond this point. This rise is due to the change of slope in the mass-luminosity relation at $M_V \sim 8$ for solar chemistry (see e.g., D'Antona 1998), which can also be seen as a change in slope in the cluster main-sequence (see §3.4.2 or CMD figures). Integrating the luminosity function and

accounting for red giants and white dwarfs provides a lower limit to the total cluster population of ~ 2600 stars (this value is corrected for stars down to the H-burning limit in §7). This observed NGC 2099 stellar content makes it very similar to that of NGC 6819 (2900 observed stars), and therefore one of the richest open star clusters known.

In Figure 11 we compare the NGC 2099 luminosity function to that for the Solar Neighborhood (Binney & Merrifield 1998), the Pleiades (Lee & Sung 1995) and NGC 6819 (Paper II). We have normalized the luminosity functions to the number of stars in NGC 2099 at the $M_V = 5$ bin. The masses of the stars in this bin are slightly less than solar and no stellar evolutionary effects have yet taken place for any of the clusters. The luminosity function for NGC 2099 exhibits a similar slope to both the Pleiades and the Solar Neighborhood from $M_V = 6 - 10$. The cluster NGC 6819 is 10 times older than its relaxation time and therefore has lost some of its low-mass, faint stars (see Paper II).

5.3. Mass Segregation

Mass segregation is a consequence of dynamical evolution where evaporation and redistribution of low mass stars may have occurred in the cluster. Although this process has been known to occur in open clusters as early as 1960 (van den Bergh & Sher), one of the first efforts to catalogue dynamical effects in many open clusters occurred when Francic investigated mass functions of eight clusters (Francic 1989). Francic's study clearly showed that the effects of mass segregation are more prominent in older clusters. Other recent studies have also confirmed that the mass functions for some open clusters have likely changed over time due to dynamical evolution (for example the Hyades (Reid 1992); NGC 188 (von Hippel & Sarajedini 1998); Praesepe and NGC 6231 (Raboud & Mermilliod 1998); NGC 2420 (Lee, Kang & Ann 1999); NGC 2516 (Hawley, Tourtellot & Reid 1999); M11 (Sung et al. 1999); M35 (Barrado y Navascues et. al. 2001); the Pleiades (Adams et al. 2001); NGC 6819 (Kalirai et al. 2001b)). Some of these clusters are quite young, such as the Pleiades, but others such as NGC 2420 and NGC 6819 are several billions of years old. We should also mention that Sagar & Griffiths (1998) looked at mass segregation effects for five, distant open clusters and found that the effects are not correlated with cluster age. NGC 2099 is an ideal cluster for dynamical studies as it is neither very old nor very young but rather splits the above sample in age. It is also an excellent candidate as it is several times richer than most of the above clusters.

A good method to test these evolutionary effects is to compare the luminosity (or mass) functions in increasing concentric annuli from the center of the cluster. We split the cluster into four annuli, each $3.5'$ in radial extent, with geometry summarized in Table 5. Figure 12 displays luminosity functions in each annulus, scaled to the number of stars at $M_V = 5$. Although not as prominent as in NGC 6819, there is some evidence for mass segregation of the faintest stars in NGC 2099 (cluster age $\sim 1.7 \times$ dynamical age). The outer annuli of the cluster show a greater relative concentration of lower mass stars ($0.40 M_\odot - 0.60 M_\odot$).

6. Mass Functions

We have used the slope of the M_V –mass relation from our theoretical isochrone (520 Myrs) to convert the observed luminosity function into a mass function in an identical manner to that described in Paper II for NGC 6819. The mass function represents the number of stars / unit mass in the cluster. Typically, the mass function is assumed to be a power law so that

$$\Psi(m) \propto m^{-(1+x)}, \quad (3)$$

where x takes on a value of 1.35 in the work of Salpeter (1955). For the first cluster in our survey, NGC 6819, we found that the best fit power law slope was $x = -0.15$, i.e. the mass function is very flat. This was expected as the cluster was 10 times older than its relaxation time. We can also summarize the results of Francic (1989) who demonstrated that the mass functions for some old Galactic clusters (NGC 6633, NGC 752, and M67) are dominated by higher mass stars. This analysis also showed that the slope of the mass function for younger open clusters was $x \sim 1$. The inverted mass function for the older clusters is thought to be due to dynamical processes in the cluster that work to evaporate low mass stars and retain the higher mass stars. We have shown that it is likely that these processes may have already occurred in NGC 2099 (see §§5 and 5.3). NGC 2099 is only about 1.7 times older than its dynamical relaxation time, and therefore should exhibit a much steeper global mass function than what was observed in NGC 6819 if all clusters form initially with a mass function slope near that of a Salpeter value. Figure 13 shows the mass function for the cluster (solid) and a Salpeter slope (dashed). This mass function extends from $\sim 0.3 M_{\odot}$ (the limit of our photometry) to $\sim 2.6 M_{\odot}$ (the main-sequence turn-off) and has a best fit slope of $x = 0.60$ between $\sim 0.5 M_{\odot}$ and $\sim 1.8 M_{\odot}$, somewhat flatter than the Salpeter value. The high mass end of the mass function (between $\sim 1.8 M_{\odot}$ and $\sim 2.6 M_{\odot}$) is much steeper with a best fit slope of $x = 2.5$. The two lowest mass bins ($\sim 0.3 M_{\odot}$ to $\sim 0.5 M_{\odot}$) of the mass function show a very flat distribution. For such low masses, color transformation equations are not available for the non-grey boundary conditions used in our models, however, we have extrapolated a mass-luminosity relation (as discussed in §3.4.1). Integrating the global mass function, and accounting for the evolved stars, provides a total cluster mass of $\sim 2300 M_{\odot}$.

7. Star Counts Down to the H-burning Limit

Both the estimated total cluster population (~ 2600 stars) from §5.2 and the total cluster mass ($\sim 2300 M_{\odot}$) from §6 are lower limits due to our photometric limit ($V \sim 23.5$ on the main-sequence). To obtain a more realistic measure of the total cluster population (which is required in the estimates of the dynamical time and tidal radius), we extrapolate our observed luminosity function to the hydrogen burning limit. The counts between our faintest bin ($\sim 0.30 M_{\odot}$) and the hydrogen burning limit ($0.08 M_{\odot}$) are obtained by normalizing the Pleiades luminosity function (Lee & Sung 1995) to the NGC 2099 function (see Figure 11). The results provide an additional 1350 stars with a

total mass of $210 M_{\odot}$. This raises the NGC 2099 cluster population to just under 4000 stars and a total cluster mass of just over $2500 M_{\odot}$. We also note that the total mass of the cluster may be larger due to the presence of binary stars. The total cluster population may also be higher due to the missed stars between our cluster extent and the tidal radius.

8. White Dwarfs in Open Clusters

As mentioned in §1, observations of white dwarfs in Galactic open clusters have been limited for several reasons. The only major large scale observational program to attack issues such as the initial-final mass relationship and upper mass limit to white dwarf production in open clusters has been the almost two decade-long study of Dieter Reimers and Detlev Koester (see Reimers & Koester 1988b for an early summary). The study of these two relations is very important in order to better understand both post main-sequence evolution and the chemical evolution of the disk of our Galaxy. For example, the initial-final mass relationship depends on the history of stellar mass loss in post main-sequence evolutionary stages. The techniques to be used to establish constraints on these two relations are a lot simpler than other semi-empirical methods due to large observational and theoretical uncertainties. For example, neutron star birth rates versus white dwarf birth rates can be used to determine the upper mass limits for these stars, as can the statistics of supernova explosions.

We will use our rich CMD and white dwarf cooling models to establish a statistical location for white dwarfs in our CMD. The cooling models will yield a preliminary value for the final masses of the stars and, when combined with the luminosity of the star, will provide a white dwarf cooling age. We can then use the cluster age to determine the main-sequence lifetime for each of the progenitor stars to the white dwarfs. Finally, main-sequence stellar evolutionary models will be used to provide initial masses for these stars. The largest uncertainty in the above analysis is determining accurately the final masses of the white dwarfs. First, we do not know exactly which objects are bona-fide cluster members, and secondly, the objects do not closely follow any particular mass cooling sequence. The current project will therefore identify possible candidates that will then be spectroscopically observed using multi-object spectrographs on 8-meter class telescopes to isolate cluster members and measure surface gravities and effective temperatures (which gives a more accurate value of the final mass). This is a similar approach to that of Reimers and Koester who used spectroscopy to confirm and identify bright white dwarfs (individually) in sparsely populated open clusters that had been discovered in previous published imaging projects. Only a few objects were found in each study and the results for all clusters were combined to establish constraints on the relationships outlined above. Among the clusters studied were NGC 2516 (Koester & Reimers 1996; Reimers & Koester 1982), NGC 6633 (Reimers & Koester 1994), NGC 3532 (Koester & Reimers 1993), NGC 2168 (Reimers & Koester 1988), IC 2391 and NGC 2451 (Koester & Reimers 1985), and NGC 2287 and NGC 2422 (Koester & Reimers 1981).

The clusters studied by Reimers and Koester do not generally contain enough white dwarfs to

accurately establish a cooling sequence and therefore, an independent age measurement. However, white dwarf cooling ages have been established for older open star clusters such as M67 (Richer et al. 1998) and NGC 2420 (von Hippel & Gilmore 2000). The difficulties in these studies are that the photometry does not extend much fainter than the end of the cooling sequence and that the termination of the white dwarf cooling sequence is buried in field stars or unresolved galaxies making it very difficult to actually isolate it on the CMD. The statistics in these clusters do show that the end of the cooling sequence has been detected, but these are affected by large errors.

Clusters such as NGC 2099 and NGC 6819 (Paper II) possess advantages over both the young clusters studied by Reimers and Koester and these older clusters. NGC 2099 is several times richer than any of the younger clusters and the photometry is both more accurate and deeper. Therefore, spectroscopic observations of the objects in this cluster will not only increase the sample size by many factors, but also establish constraints from fainter, older white dwarfs. The cluster is also approximately three times richer than the richest of the older clusters for which a white dwarf cooling age has been established. The white dwarf population is also well separated from the bulk of the field stars thereby making the statistics simpler. Additionally, our photometry extends almost 1.5 magnitudes fainter than the termination of the white dwarf cooling sequence and the cluster CMD clearly shows that we have detected the end of the cooling sequence. A disadvantage of studying white dwarfs in NGC 2099 rather than M67, NGC 2420 and NGC 6819 is that the cluster is not yet old enough for a long trail of white dwarfs to have formed so it is difficult to fit a cooling model over a wide magnitude range of white dwarfs.

8.1. Removing Non-cluster Objects

The background field CMD (Figure 3) shows that there is a significant population of field stars and/or faint background galaxies in the region where cluster white dwarfs are expected (see $22 \leq V \leq 25$, $0 \leq B-V \leq 0.6$). However, this population is also clearly more dense in the cluster field. Although we can not delineate those objects that are cluster members from the CMD alone, we can use the background field to statistically determine the number of expected cluster members and their most likely location in the CMD. We count all objects in the background field within each 0.50 magnitude interval in V and remove 1.37 times the number of field objects in the same magnitude bin. This approach is only invoked for possible white dwarfs in the faint, blue end of the CMD. It is important to note that we may in fact remove all white dwarf candidates in this process if there were no cluster white dwarfs. This statistical technique no longer allows us to consider individual objects as potential white dwarfs: multi-object spectroscopy of all potential candidates, before any cuts, with instruments such as GMOS on Gemini North or LRIS on Keck, will provide the definitive answer as to which objects really are white dwarfs. If we assume that the clustering properties of background galaxies is almost uniform across the $42' \times 28'$ field, then this statistical subtraction should also eliminate the correct number of galaxies from the cluster field.

It is difficult to estimate which stellarity cut is an optimal separation of galaxies from stars, so

we must consider the expected number of galaxies in our cluster field ($R \leq 13.9$). This is done by considering galaxy counts (Woods & Fahlman 1997) at high latitude and correcting for extinction in our field. Based on these statistics and prior to any stellarity cut, there are far more objects in the brightest of our faint magnitude bins than the number of expected galaxies. For example, we expect less than 15% of all objects to be galaxies for $21 \leq V \leq 22$. However, for $22 \leq V \leq 23$, we expect 37% of our objects to be galaxies, and for $23 \leq V \leq 24$ fully 98% of our objects are expected to be galaxies. Remarkably, invoking a 0.50 stellarity cut removes approximately the correct number of galaxies from two of these three bins. For $21 \leq V \leq 22$, we expect 336 galaxies in our cluster field and we remove 430 objects with a 0.50 stellarity cut. For the $22 \leq V \leq 23$ bin, the number of objects removed at a 0.50 stellarity cut is 1015 and the number of galaxies is 1016. For $23 \leq V \leq 24$, the number of objects removed at a 0.50 stellarity cut is 1774 and the number of expected galaxies is 2552. A 0.75 stellarity cut in this last bin is almost perfect in eliminating the correct number of objects. It eliminates 2556 of the expected 2552 galaxies. Perhaps after the study of many clusters in the survey we can establish with certainty the correct stellarity cut for separating galaxies from stars, at a given signal-to-noise ratio. For this work, we will use a 0.50 stellarity cut which is the same result found for the photometry of NGC 6819 in Paper II.

After statistical subtraction as described above, most of the remaining objects in the faint-blue end of the CMD should be white dwarfs. There may also be some unresolved galaxies or field blue objects. We can estimate the number of expected field white dwarfs and compare this value to the number of faint-blue objects in our field. We use the hot white dwarf luminosity function (Figure 2 in Leggett, Ruiz & Bergeron 1998, taken from Liebert, Dahn & Monet 1988) to count the number of expected white dwarfs per pc^3 above our limiting magnitude. First, a white dwarf cooling model for $0.70 M_\odot$ (Wood 1994) is used to convert our absolute magnitude bins to bolometric magnitude bins. This then provides a value for the bolometric luminosity of the white dwarfs at each bin center. The number of expected white dwarfs, above that luminosity in that bin, simply follows from the Figure. Adding up the numbers in the bins from $M_V = 10.5$ to 13 and multiplying by the volume created by the cone that represents our cluster field, yields a population of 63 expected field white dwarfs. The number of objects in our background field, after correcting for incompleteness in our data and removing background galaxies, is 35, which when scaled up to match the size of the cluster field gives 48. The difference between the expected and the observational values can be most likely attributed to errors in the galaxy counts and therefore in the stellarity cut used and also to white dwarfs that are in binaries and therefore missed in our study (see next section).

8.2. White Dwarfs in Binaries

Evidence supporting a population of white dwarfs in binaries in NGC 2099 is provided from a very crude estimate of the expected number of white dwarfs in the cluster based on an extrapolation of the observed mass function at the high mass end. As mentioned in §6, the high mass end slope of the mass function is $x = 2.5$. Using the number counts in the $m = 2.22 M_\odot$ mass bin to solve

for the proportionality constant ($A = 3684$), and integrating equation 3 from the turn-off ($M \sim 2.6 M_{\odot}$) to the upper limit to white dwarf production ($M \sim 7 M_{\odot}$) provides a value for the expected number of white dwarfs in the cluster to be 113. This value is ~ 2 times greater than the number of detected white dwarfs (see next section). A significant number of these missing white dwarfs are most likely in main-sequence binaries, however, a few additional arguments can also help explain the discrepancy.

First, the cluster will lose stars through tidal stripping and evaporation. The white dwarfs may be more prone to these effects because of the planetary nebulae stage. Any asymmetric mass-ejection would induce a recoil velocity on the white dwarf that could kick it out of the cluster. Another effect that could possibly lead to fewer detected white dwarfs is relaxation (see §§5 and 5.3). Since the white dwarfs have a small mass compared to their progenitors, relaxation could increase their velocity dispersion and therefore make them less frequent in the cluster center (compared to the progenitors) and more susceptible to evaporation. This effect could not however be very dramatic as the white dwarf cooling ages for most of the candidates are comparable to the relaxation age for the cluster.

8.3. White Dwarf Luminosity Function and Cooling Age

For those objects that have survived the criteria outlined in §8.1, we construct a white dwarf luminosity function by binning the objects in 0.50 magnitude intervals and subtracting the background field numbers from the cluster field numbers after accounting for the 1.37 aerial difference. Figure 14 shows this result, after accounting for incompleteness corrections as described in §5.1 and summarized in Table 3. There is a clear increase in the number of stars as a function of magnitude and then a sharp turn-off at $V = 23.5$ ($M_V = 11.95 \pm 0.30$) (see Table 6). The uncertainty in this value is discussed in detail in the next section. We interpret this turn-off to represent the end of the white dwarf cooling sequence in NGC 2099. The total number of white dwarfs in NGC 2099, found from adding up the bins in the luminosity function, is 50. The bright magnitude slope of the luminosity function is in excellent agreement with the expected slope of the white dwarf luminosity function from theory (Liebert, Dahn & Monet 1988). We can use the magnitude of the termination point of the white dwarf cooling sequence to establish a lower limit to the age of NGC 2099 based on white dwarf cooling models (Wood 1994). Figure 15 shows a $0.70 M_{\odot}$ cooling model superimposed on the cluster CMD. The age from the limiting magnitude in this cooling sequence is 516 ± 154 Myrs. This age is a lower limit because it represents the time taken for the most massive progenitor stars in the cluster to cool to the limiting white dwarf magnitude and does not include the time that these stars spent on the main-sequence. The latter, for $7 M_{\odot}$ stars, is 50 Myrs, therefore raising the white dwarf cooling age of the cluster to 566 ± 154 Myrs which is in excellent agreement with the core-overshooting turn-off age (520 Myrs). Finally, we note that if we assume a slightly higher mass for the white dwarfs by $0.10 M_{\odot}$, the age decreases slightly (530 Myrs) and is in better agreement with the turn-off age. Surprisingly, the cooling ages determined

here are insensitive to the stellarity cut (0.50 or 0.75). The peak in the white dwarf luminosity function occurs at $M_V = 11.95$ independent of a 0.50 or 0.75 stellarity cut. The number of objects however, will clearly be less in the 0.75 case. This is in part due to the resolution of the bins used for the white dwarf luminosity function.

8.4. Evaluation of Errors

In order to compare the white dwarf cooling age with the main-sequence turn-off age, we must provide a careful account of all errors. As mentioned in §3.3, the total error contribution to the true distance modulus includes four terms. Additionally, the error in the limiting white dwarf cooling magnitude must also include the bin uncertainty (± 0.25 magnitudes) from Figure 14. We can address each of the uncertainties individually and then combine them correctly to account for correlations between the cross terms:

- 1.) There is an error in the vertical shift caused by the error in the horizontal shift due to $\Delta_{E(B-V)}$. This error is proportional to $\Delta_{E(B-V)}$ and to the slope of the main-sequence at the fitting point ($S = \Delta V / \Delta(B - V) \sim 5.7$). Therefore, $\Delta_A = S\Delta_{E(B-V)} = 0.17$.
- 2.) There also exists a judgement uncertainty in the vertical shift needed to superimpose the Hyades main-sequence on the NGC 2099 main-sequence at a fixed value of $E(B-V)$. Under some circumstances, this shift is very hard to determine due to large photometric spread in the main-sequence and the smearing effect of binaries. Given the tightness of the two main-sequences, we estimate this error to be quite small, $\Delta_B = 0.07$.
- 3.) The third error we consider is the error in the extinction (Δ_{A_V}) caused by the uncertainties in both the reddening ($\Delta_{E(B-V)}$) and Δ_{R_V} . This term is evaluated as

$$\Delta_C = \Delta_{A_V} = A_V \sqrt{\left(\frac{\Delta_{R_V}}{R_V}\right)^2 + \left(\frac{\Delta_{E(B-V)}}{E(B - V)}\right)^2}, \quad (4)$$

where we take $\Delta_{R_V} = 0.20$. The above equation gives $\Delta_C = 0.10$.

- 4.) The final term in our distance modulus error budget accounts for the small color shift caused by the metallicity uncertainty of the cluster. As described in §3.2, the metallicity is believed to be $Z = 0.02$. If we assume an uncertainty $\Delta_Z \sim 0.005$ (this allows the cluster metallicity to be equal to that of the Hyades), then the corresponding shift in color is $\Delta_{B-V} = \Delta_D = 0.03$.

We combine the above errors by writing the total error as a sum of these terms and then taking the mean and root as shown here:

$$\begin{aligned}
 \Delta_{(m-M)_0} &= \langle (\Delta_A + \Delta_B + \Delta_C + \Delta_D)^2 \rangle^{1/2} \\
 &= \langle \Delta_A^2 + \Delta_B^2 + \Delta_C^2 + \Delta_D^2 + 2\Delta_A\Delta_B + 2\Delta_A\Delta_C \\
 &\quad + 2\Delta_B\Delta_C + 2\Delta_A\Delta_D + 2\Delta_B\Delta_D + 2\Delta_C\Delta_D \rangle^{1/2}. \tag{5}
 \end{aligned}$$

Next, we can eliminate three of the six cross terms, $2\Delta_A\Delta_B$, $2\Delta_B\Delta_C$ and $2\Delta_B\Delta_D$, because they are the products of un-correlated errors; they are defined at fixed $E(B-V)$ so $\Delta_{E(B-V)}$ does not enter into these terms. Finally, we note that one of the cross terms, $2\Delta_A\Delta_C$, is negative because the two errors compensate for each other. An error in $\Delta_{E(B-V)}$ in one of the terms opposes the associated error caused by the $\Delta_{E(B-V)}$ in the other term. Evaluating equation 5 with these modifications gives a total error value of 0.16 on the true distance modulus.

The error in the limiting white dwarf magnitude can be found by simply adding this distance modulus error (± 0.16) in quadrature with the binning error (± 0.25). The result gives ± 0.30 .

8.5. Summary of White Dwarf Studies

This project has allowed us to identify 50 white dwarf candidates in NGC 2099. These objects have all passed a stellarity and a statistical subtraction cut. Furthermore, the bright end slope of the white dwarf luminosity function agrees well with theoretical expectations. The turn-over in the white dwarf luminosity function provides an age measurement for the cluster ($566 \pm \frac{154}{176}$ Myrs) which is in excellent agreement with the main-sequence turn-off age (520 Myrs) for a core-overshooting model. A non core-overshooting age of ~ 300 – 350 Myrs for NGC 2099 can therefore be ruled out with some certainty. The approach that we have used to estimate these quantities is a purely statistical method that needs further work. Fortunately, new multi-object spectrometers will allow us to simultaneously measure spectra for a large number of objects. We will eventually obtain spectra for all objects in the faint, blue end of the CMD before any cuts have been made. This will then provide a true measure of the number of white dwarfs in NGC 2099. Accurate surface gravities and effective temperatures for the brighter objects will provide crucial mass information which, when coupled with theoretical models, provides progenitor mass information. This will lead to a better understanding of the initial-final mass relationship for white dwarfs.

9. Conclusion

We have used deep CFH12K photometry to establish the white dwarf cooling age of one of the richest open star clusters, NGC 2099. The white dwarf luminosity function for the cluster shows a steep turn-over at $M_V = 11.95 \pm 0.30$, which is the limit to which the most massive progenitor stars have cooled to. After accounting for the main-sequence lifetime of these stars, the cooling age

is determined to be 566 ± 154 Myrs, and therefore is in excellent agreement with the main-sequence turn-off age (520 Myrs). In order to have consistency between the two ages, core-overshooting models are preferred. The $V, B-V$ CMD for NGC 2099 exhibits a spectacularly rich, long (over 12 magnitudes) and very tightly constrained main-sequence. Main-sequence fitting of the un-evolved stars in the cluster with the Hyades cluster indicates a true distance modulus of $(m-M)_0 = 10.90 \pm 0.16$ and a reddening value of $E(B-V) = 0.21 \pm 0.03$. After accounting for small metallicity differences, the slope changes in the NGC 2099 main-sequence are found to be matched almost perfectly to those in the Hyades cluster. A theoretical stellar isochrone with $Z = 0.020$ and age = 520 Myrs models several features of the CMD very well, such as slope changes in the upper main-sequence and the red giant clump. The lower main-sequence and the turn-off are found to be slightly redder than the isochrone. The radial distribution of stars in NGC 2099 are in good agreement with a single mass King model. The global luminosity function is found to be flat from $M_V \sim 2$ to $M_V \sim 8$ with a subsequent rise for fainter stars. After accounting for stars between our faintest magnitude bin and the hydrogen burning limit, the total cluster population of NGC 2099 is determined to be just under 4000 stars. Although not as severe as for the older cluster NGC 6819, we find some evidence for mass segregation within NGC 2099. The global mass function is shallower than a Salpeter IMF, and when extrapolated to the hydrogen burning limit provides a lower limit (excluding binaries and stars out to the tidal radius) to the total cluster mass of $\sim 2515 M_\odot$.

We wish to thank J. Montalban for helpful discussions concerning the modelling of low mass main-sequence stars and S. Courteau for helpful discussions concerning error analysis. The author would also like to thank the Canada-France-Hawaii Telescope Corporation for a generous three night observing run with their facility and the CFHT Corporation and Osservatorio Astronomico di Roma for accommodations and access to computing facilities during this project. The author received financial support during this work through an NSERC PGS-A research grant. The research of HBR and GGF is supported by the Natural Sciences and Engineering Council of Canada.

REFERENCES

Adams, J.D., Stauffer, J.R., Monet, D.G., Skrutskie, M.F. & Beichman, C.A. 2001, AJ, 121, 4, 2053

Barrado y Navascues, D., Stauffer, J.R., Bouvier, J. & Martin, E.L. 2001, ApJ, 546, Iss. 2, 1006

Becker, W. 1948, Astr. Nach., 276, 1

Becker, W. & Svolopoulos, S. 1976, A&AS, 23, 97

Bertelli, G., Bressan, A., Chiosi, C., Fagotto, F. & Nasi, E. 1994, A&A, 106, 275

Bertin, E. & Arnouts, S. 1996, A&AS, 117, 393

Bessell, M.S., Castelli, F. & Plez, B. 1998, A&A, 333, 231

Binney, J. & Merrifield, M. 1998, Galactic Astronomy, (Princeton: University Press)

Binney, J. & Tremaine, S. 1987, Galactic Dynamics, (Princeton: University Press)

Bolte, M. 1989, ApJ, 341, 168

de Bruijne, J.H.J., Hoogerwerf, R. & de Zeeuw, P.T. 2001, A&A, 367, 111

Canuto, V.M. & Mazzitelli, I. 1992, ApJ, 389, 724

Castellani, V., Degl'Innocenti, S. & Prada Moroni, P.G. 2001, MNRAS, 320, 1, 66

Clemens, D.P. 1985, ApJ, 295, 422

Copeland, H., Jensen, J.O. & Jorgensen, H.E. 1970, A&A, 5, 12

Cuillandre, J-C. 2001, A&A, in preparation

D'Antona, F. 1998, ASP Conference Series, 142, 157

Francic, S.P. 1989, AJ, 98, 888

Freytag, B., Ludwig, H.G. & Steffen, M. 1996, A&A, 313, 497

Giebeler, H. 1914, Bonn Veroff., 12

Girardi, L., Bressan, A., Bertelli, G. & Chiosi, C. 2000, A&AS, 141, 371

Gunn, J.E. & Griffin, R.F. 1979, AJ, 84, 753

Hansen, B.M.S. 1999, ApJ, 520, 680

Hauschildt, P.H., Allard, F. & Baron, E. 1999, ApJ, 512, 377

Hawley, S.L., Tourtellot, J.G. & Reid, I.N. 1999, AJ, 117, 3, 1341

Hoag, A.A., Iriarte, B., Johnson, H.L., Hallam, K.L., Mitchell, R.I. & Sharpless, S. 1961, Pub. U.S. Naval Observatory, Ser. 2, 17 349

Iben, I. Jr. & Renzini, A. 1983, ARAA, 21, 271

Janes, K.A., Tilley, C. & Lynga, G. 1998, AJ, 95, 771

Jeffreys, W.H., III. 1962, AJ, 67, 532

Kalirai, J.S., Richer, H.B., Fahlman, G.G., Cuillandre, J., Ventura, P, D'Antona, F., Bertin, E., Marconi, G. & Durrell, P. 2001a, AJ, 122, 257

Kalirai, J.S., Richer, H.B., Fahlman, G.G., Cuillandre, J., Ventura, P, D'Antona, F., Bertin, E., Marconi, G. & Durrell, P. 2001b, AJ, 122, 266

King, I.R. 1962, AJ, 67, 471

King, I.R. 1966, AJ, 71, 276

Koester, D. & Reimers, D. 1996, A&A, 313, 810

Koester, D. & Reimers, D. 1993, A&A, 275, 2, 479

Koester, D. & Reimers, D. 1985, A&A, 153, 260

Koester, D. & Reimers, D. 1981, A&A, 99, L8

Landolt, A. U. 1992, ApJ, 104, 340

Lee, S.H., Kang, Y.W. & Ann, H.B. 1999, JKAS, 14, 2, 61

Lee, S. & Sung, H. 1995, JKAS, 28, 1, 45

Leggett, S.K., Ruiz, M.T. & Bergeron, P. 1998, ApJ, 497, 294

Liebert, J., Dahn, C.C. & Monet, D.G. 1988, ApJ, 332, 891

Lindblad, P.O. 1954, St. An., 18, 1

Mermilliod, J.C., Huestamendia, G., del Rio, G. & Mayor, M. 1996, A&A, 307, 80

Nordlund, J. 1909, Sv. Ark. Math., 5, 17

O'Brien, M.S., Vauclair, G., Kawaler, S.D., Watson, T.K., Winget, D.E., Nather, R.E., Montgomery, M., Nitta, A., Kleinman, S.J., Sullivan, D.J., Jiang, X.J., Marar, T.M.K., Seetha, S., Ashoka, B.N., Bhattacharya, J., Leibowitz, E.M., Hemar, S., Ibbetson, P., Warner, B., van Zyl, L., Moskalik, P., Zola, S., Pajdosz, G., Krzesinski, J., Dolez, N., Chevreton, M., Solheim, J-E., Thomassen, T., Kepler, S.O., Giovannini, O., Provencal, J L., Wood, M.A. & Clemens, J.C. 1998, ApJ, 495, 458

Perryman, M.A.C., Brown, A.G.A., Lebreton, Y., Gomez, A., Turon, C., de Strobel, G.C., Mermilliod, J.C., Robichon, N., Kovalevsky, J. & Crifo, F. 1998, A&A, 331, 81

Raboud, D. & Mermilliod, J-C. 1998, A&A, 333, 897

Reid, N. 1992, MNRAS, 257, 2, 257

Reimers, D. & Koester, D. 1994, A&A, 285, 451

Reimers, D. & Koester, D. 1988, A&A, 202, 1, 277

Reimers, D. & Koester, D. 1988b, ESO Messenger, 54, 47

Reimers, D. & Koester, D. 1982, A&A, 116, 2, 341

Renzini, A. & Fusi-Peccia, F. 1988, ARAA, 26, 199

Richer, H.B., Hansen, B., Limongi, M., Chieffi, A., Straniero, O. & Fahlman, G.G. 2000, ApJ, 529, Issue 1, 318

Richer, H.B., Fahlman, G.G., Rosvick, J. & Ibata, R. 1998, ApJ, 504, L91

Richer, H.B., Fahlman, G.G., Ibata, R.A., Pryor, C., Bell, R.A., Bolte, M., Bond, H.E., Harris, W.E., Hesser, J.E., Holland, S., Ivanans, N., Mandushev, G., Stetson, P.B. & Wood, M.A. 1997, ApJ, 484, 741

Sagar, R. & Griffiths, W.K. 1998, MNRAS, 299, 777

Salpeter, E.E. 1955, ApJ, 121, 161

Saumon, D. & Jacobson, S.B. 1999, ApJ, 511, L107

Schaller, G., Shaerer, D., Meynet, G. & Maeder, A. 1992, A&A, 96, 269

Sung, H., Bessell, M.S., Lee, H-W, Kang, Y.H. & Lee, S-W. 1999, MNRAS, 310, 4, 982

Upgren, A.R. 1966, AJ, 71, 8, 736

van den Bergh, S. & Sher, D. 1960, Publ. David Dunlap Obs., 2, 203

Ventura, P., Zeppieri, A., Mazzitelli, I. & D'Antona, F. 1998, A&A, 334, 953

von Hippel, T. & Gilmore, G. 2000, AJ, 120, Iss. 3, 1384

von Hippel, T. & Sarajedini, A. 1998, AJ, 116, Iss. 4, 1789

von Zeipel, H. & Lindgren, J. 1921, Sv. Vet. H., 61, N15

Weidemann, V. 2000, A&A, 363, 647

Weidemann, V. 1987, A&A, 188, 74

West, F.R. 1967, ApJS, 14, 359

Wielen, R. 1991, ASPCS, Formation and Evolution of Star Clusters, 13, 343

Wood, M.A. 1994, AAS Meeting, 185, 4601

Woods, D. & Fahlman, G. 1997, ApJ, 490, 11

Xiong, D.R. 1985, A&A, 150, 133

Zug, R.S. 1933, Lick Obs. Bull., 16, 130

Fig. 1.— Color image created from the individual V and B 300-second frames. The image size is $42' \times 28'$.



Fig. 2.— Statistical errors in the PSFex photometry. These are negligible up to $V = 22$, at which point they start rising rapidly. The mean error at $V = 23$ is 0.032 and at $V = 24$ is 0.075. Very few outliers are present in the photometry. Two small ‘glitches’ at $13 \leq V \leq 15$ and $V \sim 17.5$ indicate the magnitudes at which the different exposure time data sets were merged.

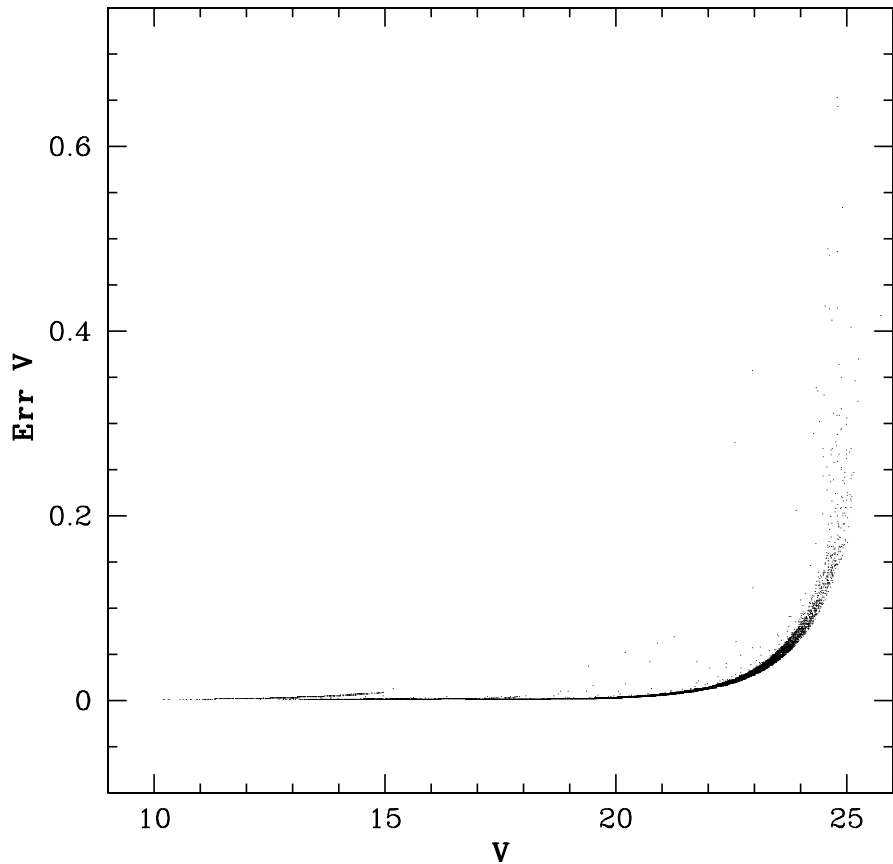


Fig. 3.— Rich, tight and long main-sequence of NGC 2099 is clearly separated from the background/foreground distribution. The cluster field has been scaled down in area by a factor of 1.37 (as described in text) so that the relative populations on the two diagrams can be compared (see Figure 5 for all stars). A 0.50 stellarity cut has been applied to both diagrams.

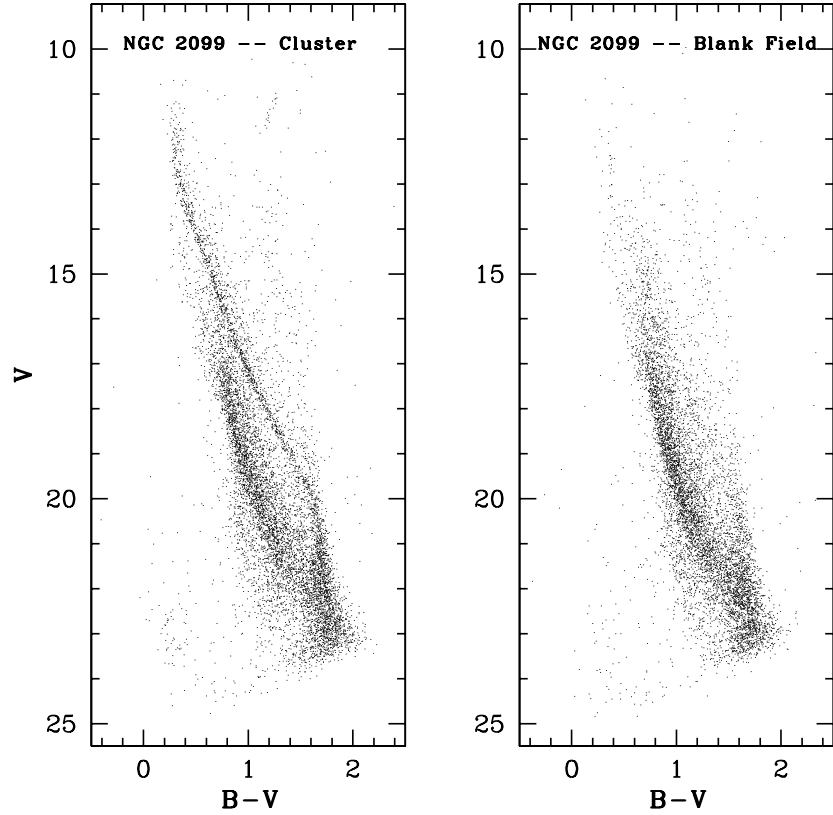


Fig. 4.— SExtractor star/galaxy classification shown for all objects in the cluster field. A number of stars (stellarity = 1) and galaxies (stellarity = 0) are clearly evident. The classification of the remaining objects is discussed in §§3.1 and 8.1.

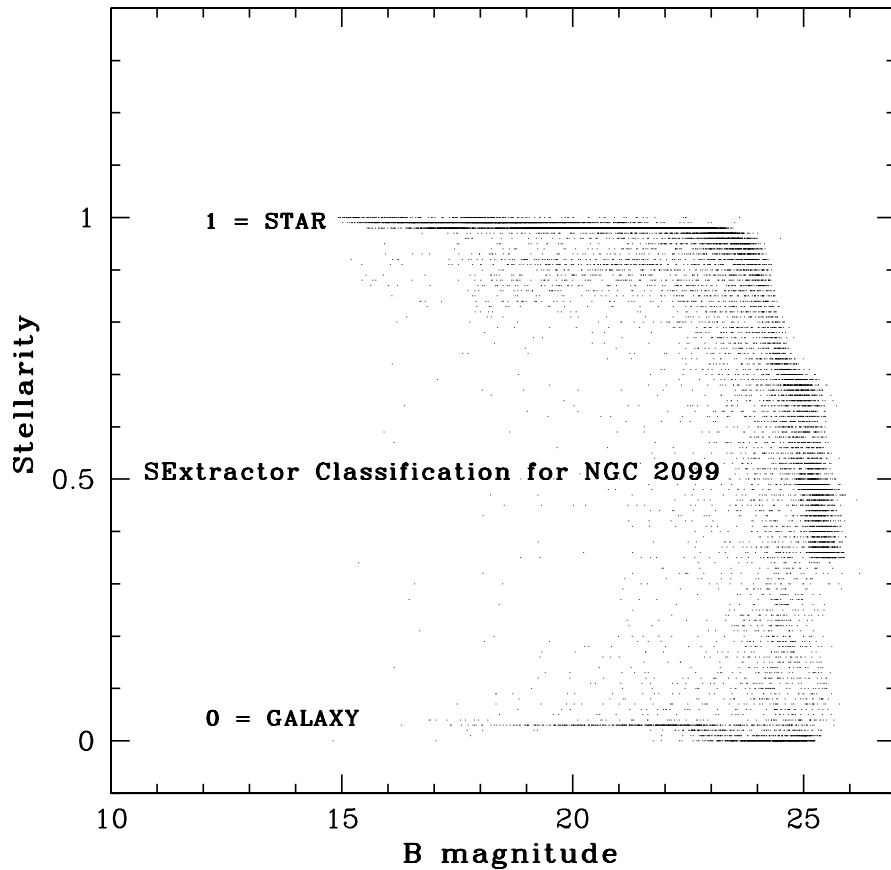


Fig. 5.— The present CCD photometry is compared to the NGC 2099 studies of West (photographic) and Mermilliod (photoelectric). Unlike Figure 3, the right hand panel here contains all cluster stars out to $R = 13'.9$.

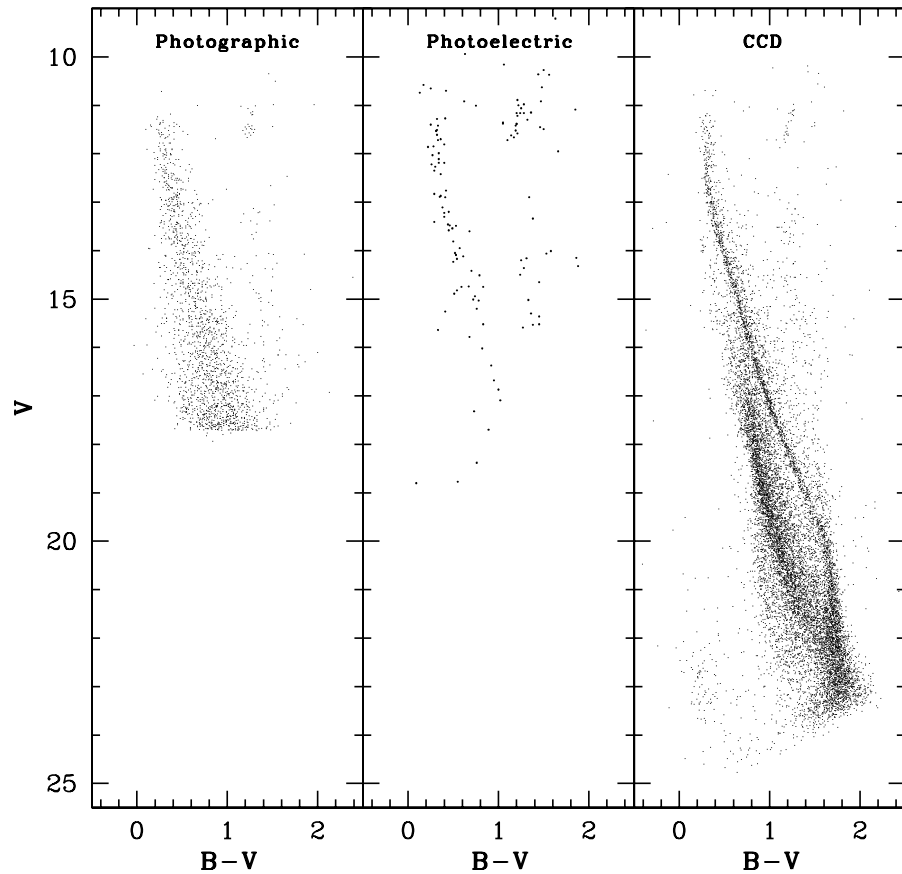


Fig. 6.— Photometric magnitudes for bright individual stars in the present CCD photometry are compared to the values obtained in the Mermilliod et al. (1996) photoelectric study. The residuals (which show CCD – photoelectric vs CCD) are found to be very small and show no obvious biases or trends. Surprisingly, the residuals are higher for brighter sources which may be due to the extremely short exposures required to measure these stars in the CCD case.

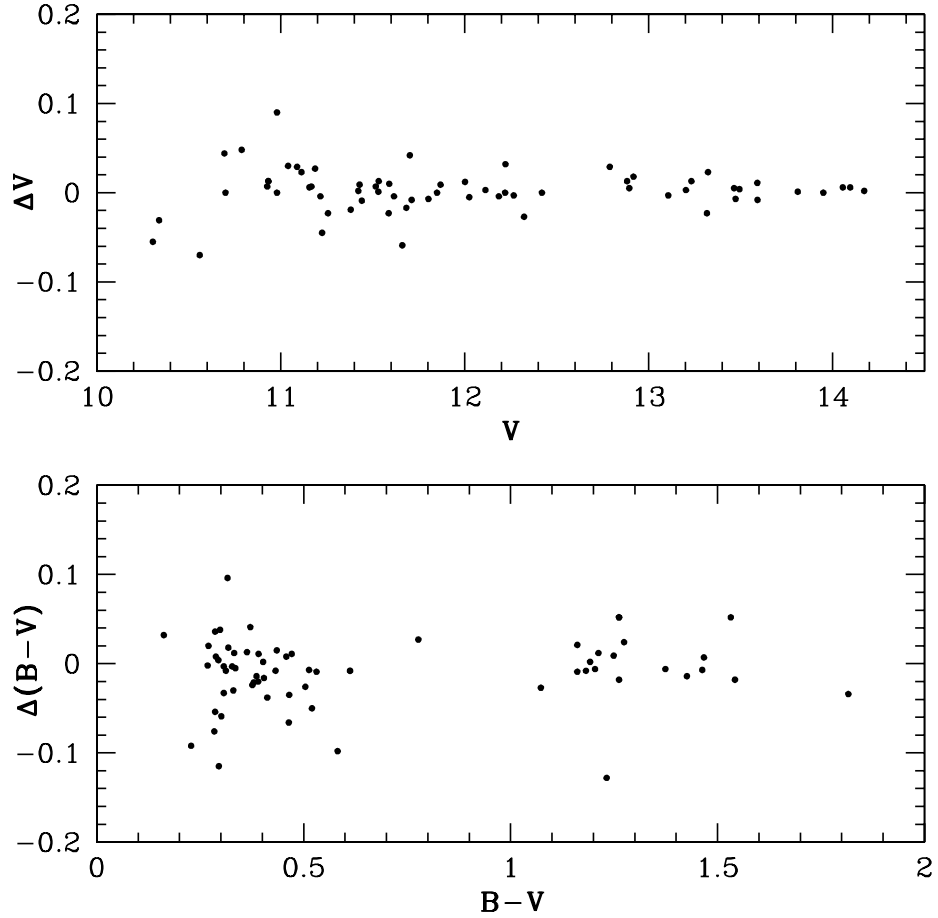


Fig. 7.— NGC 2099 main-sequence is brought to the Hyades (red points) plane by adjusting the metallicity, reddening and distance as described in §§3.2 and 3.3. The resulting detailed shape of the NGC 2099 main-sequence is found to be in excellent agreement with the Hyades cluster, thus simplifying the main-sequence fitting. The turn-off and clump stars in the Hyades clearly indicate a slightly older cluster, as confirmed by the isochrones ($\Delta\text{age} \sim 100$ Myrs).

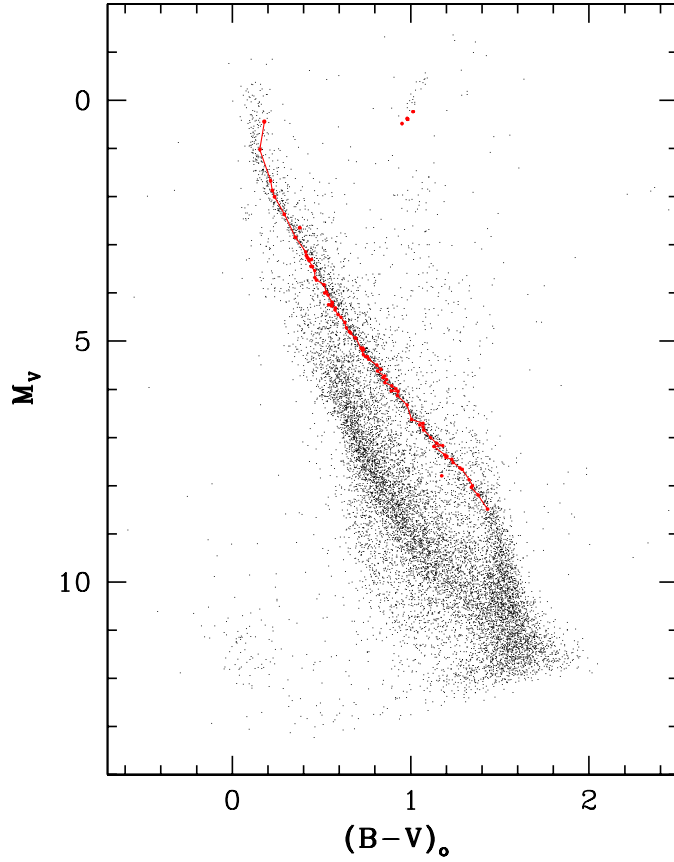


Fig. 8.— The left panel shows the best fit isochrone, based on the luminosity of the clump stars, to the observed NGC 2099 data. A better fit to the turn-off of the main-sequence is shown in the middle panel, however, a close examination of the clump stars shows a ~ 0.20 magnitude discrepancy when compared to this model. A non core-overshooting model (right panel) provides a poor fit to the data. See §3.4.2 for a discussion of these results.

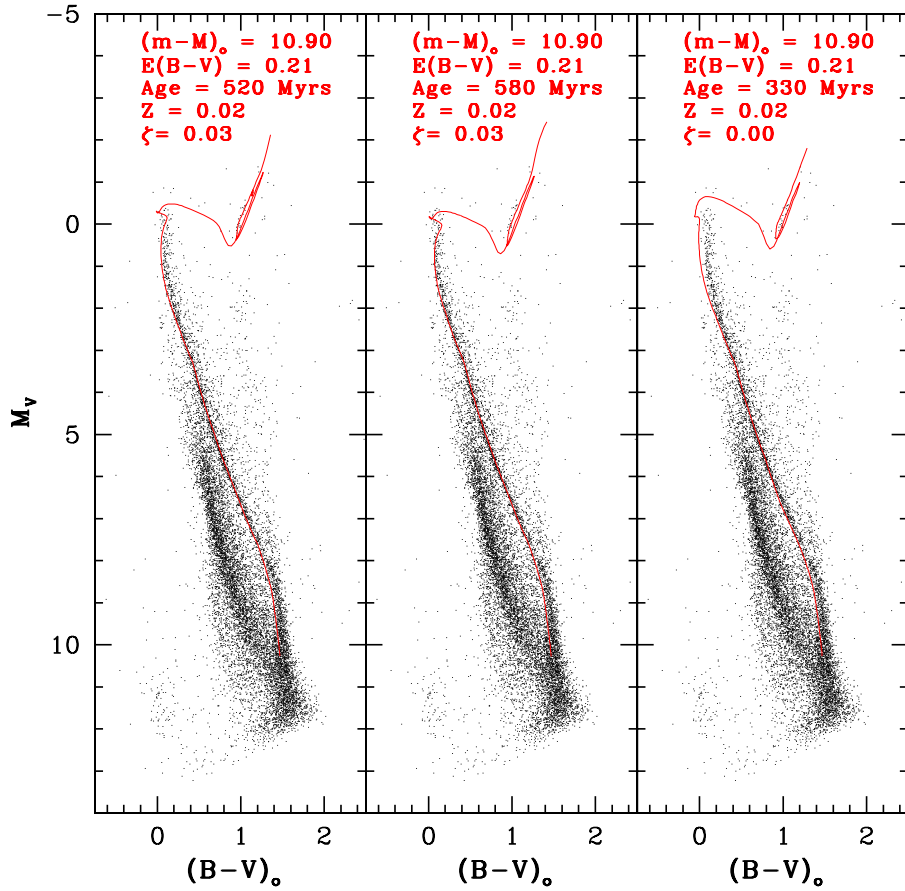


Fig. 9.— Single mass King model found to be in good agreement with the NGC 2099 radial density distribution. Only stars with $V \leq 22$ have been counted to avoid incompleteness effects. The arrows mark the core, half-mass and tidal radii of NGC 2099.

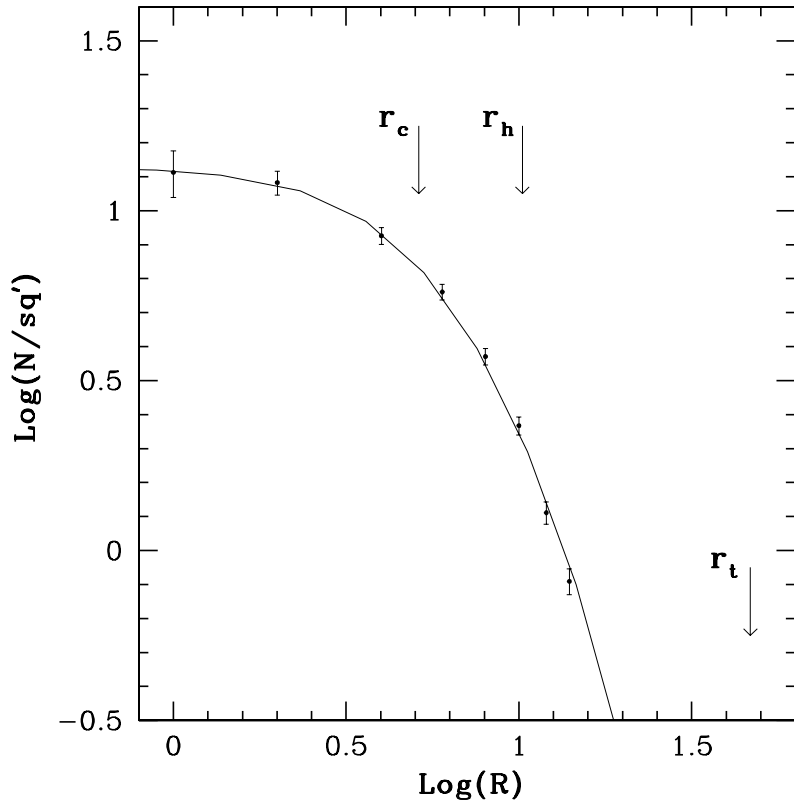


Fig. 10.— Global ($R \leq 13.9$) luminosity function is shown before (dashed) and after (solid) incompleteness corrections. The rising portion of the luminosity function beyond $V \sim 19.5$ ($M_V \sim 8$) corresponds to a slope change in the lower main-sequence of the cluster CMD, and is caused by an inflection in the mass-luminosity relationship. The error bars reflect a combination of Poisson errors and incompleteness errors as discussed in §5.1.

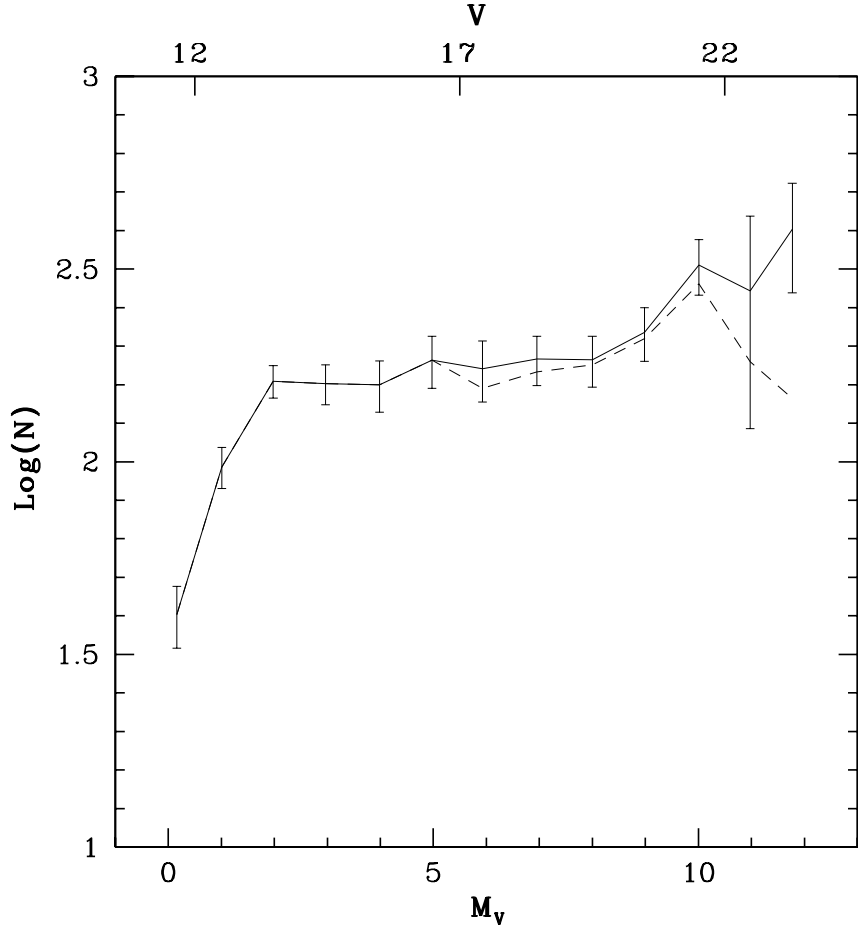


Fig. 11.— NGC 2099 luminosity function is compared with the Solar Neighborhood distribution of stars, the Pleiades luminosity function and the NGC 6819 luminosity function. All luminosity functions have been normalized to the number of stars in NGC 2099 at $M_V = 5$ to avoid evolutionary effects. NGC 6819 exhibits an inverted slope with respect to the other functions due to significant dynamical effects.

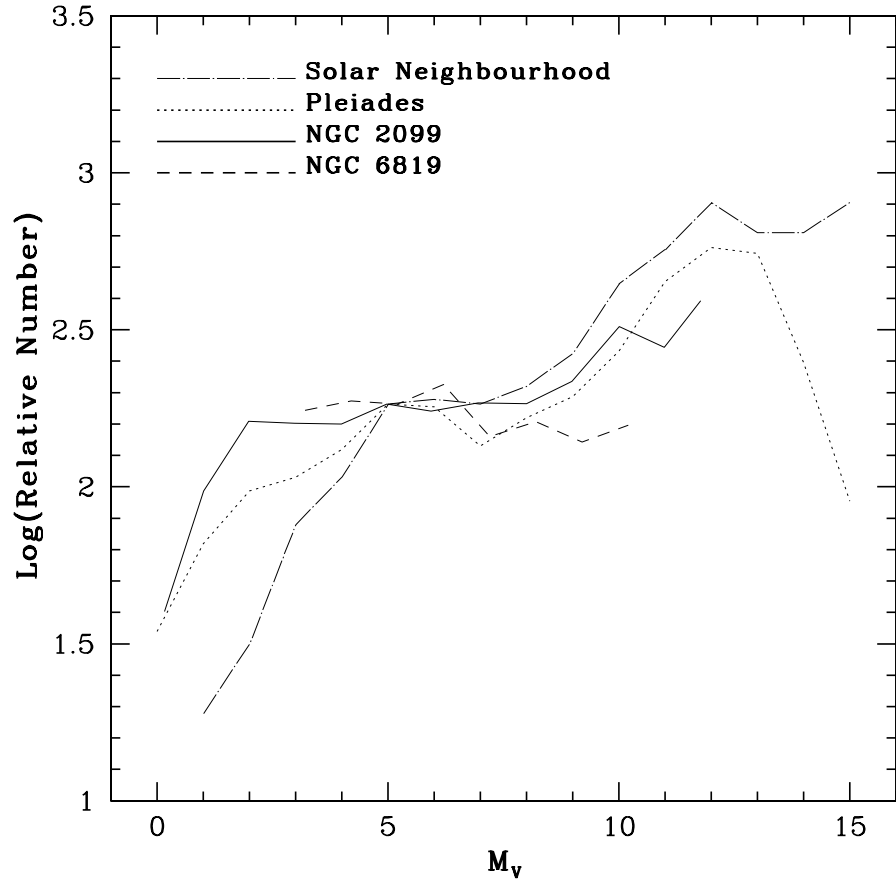


Fig. 12.— Luminosity function shown for four increasing concentric annuli around NGC 2099. The counts in all annuli have been normalized to the number at $M_V = 5$. There is some evidence for mass segregation in the faintest bins.

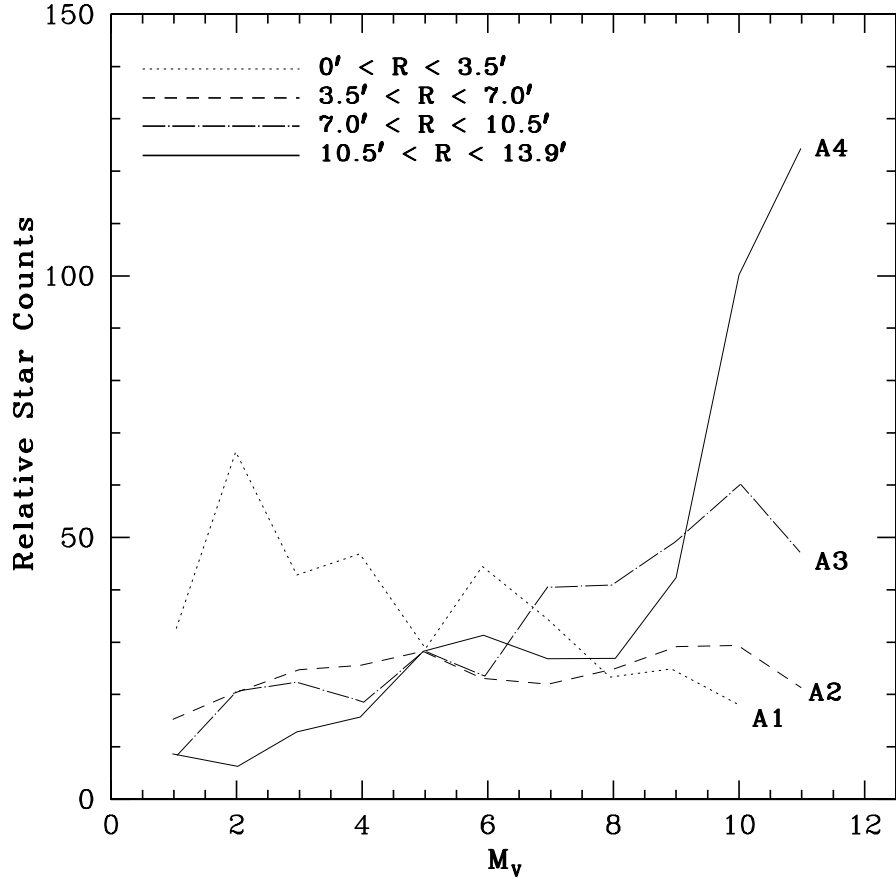


Fig. 13.— Global mass function of NGC 2099 (solid, $x = 0.60$) found to be flatter than a Salpeter IMF (dashed, $x = 1.35$) from $\sim 0.5 M_{\odot}$ to $\sim 1.8 M_{\odot}$. The slope of the high mass end of the mass function is found to be very steep, $x = 2.5$.

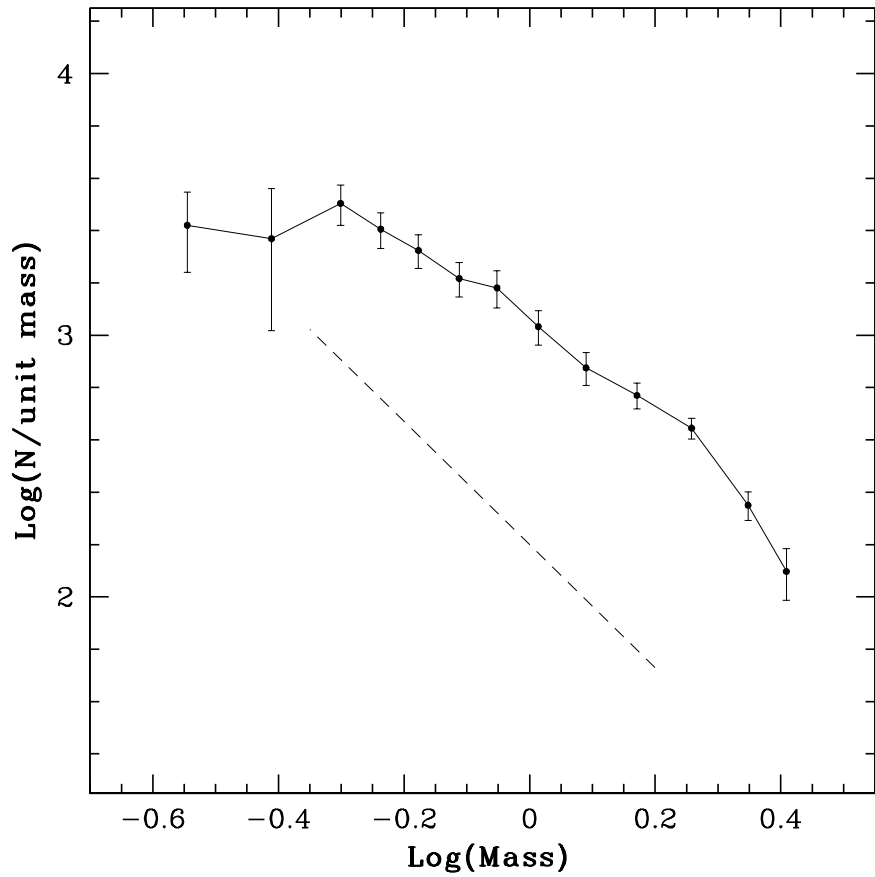


Fig. 14.— White dwarf luminosity function rises to a peak at $V = 23.5$ ($M_V = 11.95 \pm 0.30$) and subsequently drops off rapidly (see §8.4 for error analysis). The bright end slope of the luminosity function is in agreement with theoretical expectations (dashed). The errors bars include both counting uncertainties and incompleteness errors. For a $0.70 M_\odot$ white dwarf cooling sequence, the limiting magnitude of the cooling white dwarfs provides a white dwarf cooling age of $566 \pm \frac{154}{176}$ Myrs for NGC 2099. This age is in excellent agreement with the main-sequence turn-off age (520 Myrs) for a core-overshooting model.

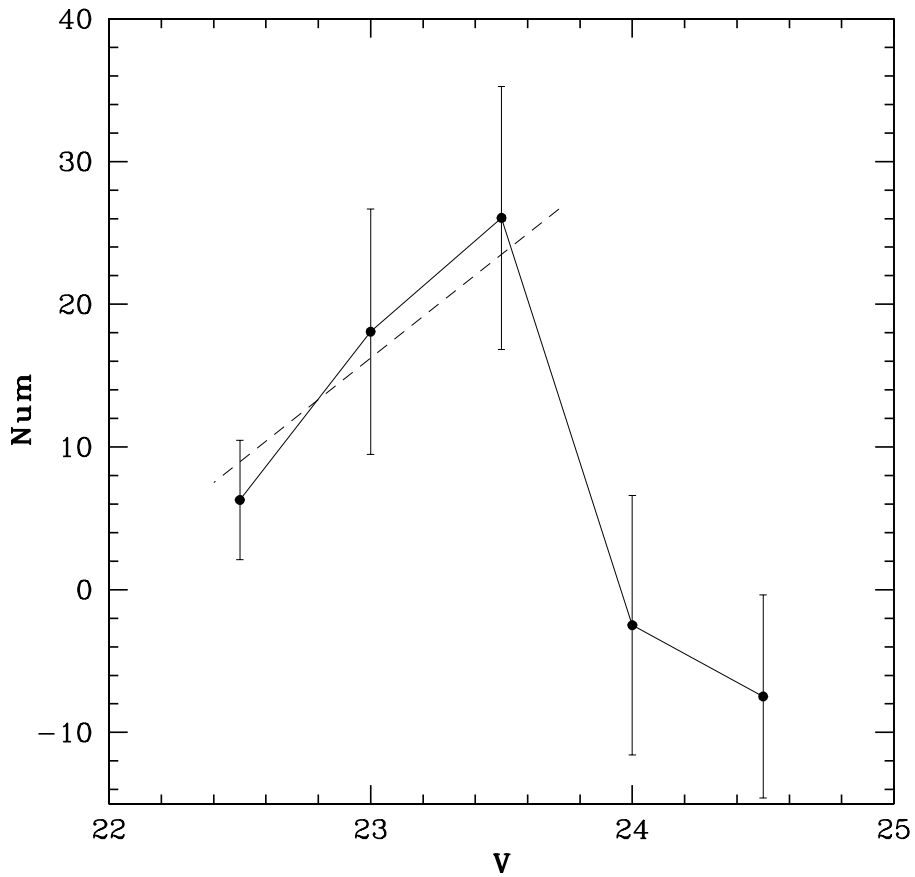


Fig. 15.— The theoretical isochrone is in excellent agreement with the data for both the red giant clump (top) and for the main-sequence from $V = 14$ to $V = 20$ (middle). The white dwarf population is clearly evident and is shown with respect to a $0.70 M_{\odot}$ white dwarf cooling sequence and the corresponding cooling ages (bottom).

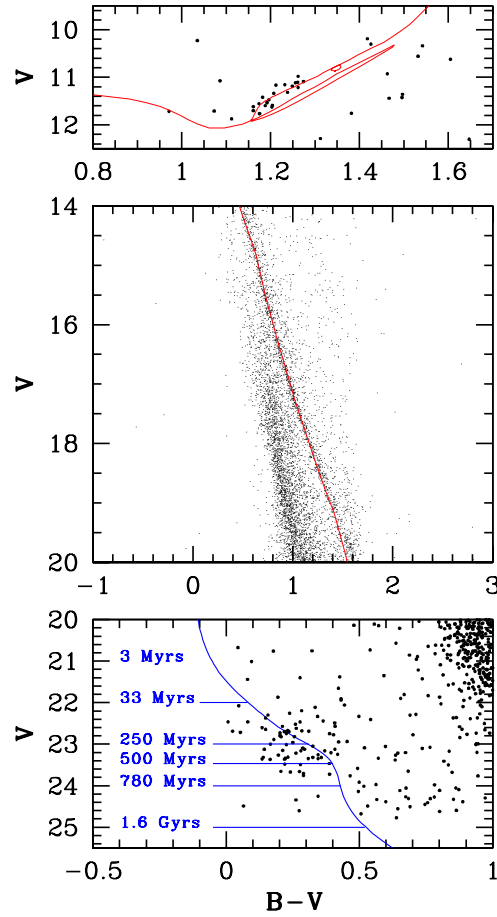


Table 1. Observational Data for NGC 2099

Filter	Exposure Time (s)	No. Images	Seeing (")	Air-mass
V	300	3	0.85	1.03
	50	1	0.97	1.04
	10	1	0.99	1.04
	0.5	1	1.1	1.19
B	300	3	0.79	1.03
	50	1	0.85	1.03
	10	1	0.85	1.03
	0.5	1	1.0	1.19
R	50	1	0.81	1.04
	10	1	0.81	1.04

Table 2. NGC 2099 Fiducial for $(m-M)_V = 11.55$, $E(B-V) = 0.21$

M_V	$(B-V)_o$
-0.20	0.066
0.23	0.082
0.70	0.082
1.22	0.106
1.70	0.149
2.20	0.219
2.70	0.304
3.20	0.417
3.74	0.485
4.21	0.551
4.73	0.626
5.21	0.711
5.70	0.800
6.19	0.891
6.71	1.011
7.22	1.125
7.70	1.216
8.19	1.321
8.69	1.401
9.22	1.462
9.72	1.474
10.22	1.495
10.71	1.517
11.20	1.556
11.69	1.589
12.12	1.600

Table 3. Completeness Corrections

V mag	No. Stars Input	No. Stars Recovered (Cluster/Background)	Completeness Correction (Cluster/Background)
Main-Sequence			
11.0-12.0	34	34/34	1/1
12.0-13.0	24	24/24	1/1
13.0-14.0	26	26/26	1/1
14.0-15.0	46	46/46	1/1
15.0-16.0	34	34/34	1/1
16.0-17.0	54	54/54	1/1
17.0-18.0	50	48/50	1.042/1
18.0-19.0	58	56/58	1.036/1
19.0-20.0	70	66/68	1.061/1.029
20.0-21.0	56	54/54	1.037/1.037
21.0-22.0	100	94/96	1.064/1.042
22.0-23.0	78	64/66	1.219/1.182
23.0-24.0	100	72/84	1.389/1.190
24.0-25.0	62	36/50	1.722/1.240
White Dwarfs			
21.0-22.0	14	13/14	1.077/1
22.0-23.0	30	26/28	1.154/1.071
23.0-24.0	38	30/32	1.267/1.188
24.0-25.0	34	20/26	1.700/1.308

Table 4. Cluster Star Counts (Raw/Corrected)

V mag	A1	A2	A3	A4	GLOBAL
11.0-12.0 (Raw)	40.1
Corrected	... (...)	... (...)	... (...)	... (...)	40.1 (7.3)
12.0-13.0 (Raw)	32.6	37.8	15.0	11.6	97.0
Corrected	32.6 (5.9)	37.8 (6.8)	15.0 (5.4)	11.6 (5.5)	97.0 (11.9)
13.0-14.0 (Raw)	66.4	50.2	36.9	8.3	161.8
Corrected	66.4 (8.5)	50.2 (8.1)	36.9 (7.9)	8.3 (6.6)	161.8 (15.6)
14.0-15.0 (Raw)	42.8	61.4	40.1	17.1	159.4
Corrected	42.8 (7.4)	61.4 (9.9)	40.1 (10.1)	17.1 (10.0)	159.4 (18.8)
15.0-16.0 (Raw)	46.8	63.5	33.2	20.9	158.5
Corrected	46.8 (8.5)	63.5 (11.9)	33.2 (12.8)	20.9 (14.1)	158.5 (24.0)
16.0-17.0 (Raw)	28.7	70.2	50.7	37.6	183.3
Corrected	28.7 (8.2)	70.2 (13.6)	50.7 (15.6)	37.6 (17.3)	183.3 (28.1)
17.0-18.0 (Raw)	41.9	52.7	36.6	34.8	155.0
Corrected	44.5 (9.4)	57.4 (13.7)	42.1 (16.0)	41.7 (18.2)	174.2 (31.4)
18.0-19.0 (Raw)	32.8	51.3	67.8	31.3	171.1
Corrected	34.4 (8.0)	54.5 (12.0)	72.6 (15.0)	35.7 (15.2)	184.8 (27.1)
19.0-20.0 (Raw)	22.6	59.9	71.1	34.7	178.3
Corrected	23.3 (7.4)	61.7 (12.7)	73.3 (15.5)	35.8 (16.0)	183.8 (27.7)
20.0-21.0 (Raw)	24.0	69.9	84.8	54.3	208.9
Corrected	24.9 (8.4)	72.5 (14.8)	88.0 (18.4)	56.3 (19.7)	216.7 (34.2)
21.0-22.0 (Raw)	16.0	65.8	96.8	119	289.5
Corrected	18.0 (11.0)	73.0 (20.3)	107.9 (26.6)	133.3 (31.4)	323.7 (53.5)
22.0-23.0 (Raw)	...	34.6	54.8	115.9	181.7
Corrected	... (...)	52.9 (39.9)	84.6 (58.6)	165.4 (76.9)	277.8 (155.9)
23.0-24.0 (Raw)	145.9
Corrected	... (...)	... (...)	... (...)	... (...)	391.2 (125.6)

Table 5. Geometry of Annuli

Annulus	Radius (')	Radius (pixels)
A1	$0 \leq R \leq 3.5$	$0 \leq R \leq 1019$
A2	$3.5 \leq R \leq 7.0$	$1019 \leq R \leq 2039$
A3	$7.0 \leq R \leq 10.5$	$2039 \leq R \leq 3058$
A4	$10.5 \leq R \leq 13.9$	$3058 \leq R \leq 4049$
Global	$0 \leq R \leq 13.9$	$0 \leq R \leq 4049$

Table 6. White Dwarf Luminosity Function

V mag	No. Stars	Error
22.5	6.3	4.2
23.0	18.1	8.6
23.5	26.1	9.2
24.0	-2.5	9.1
24.5	-7.5	7.1